14

The Use of NMR to Conduct a Microscopic Investigation of NAPL Entrapment in Porous Media

by

Rong-Tsong Horng

S.B., Geology, National Taiwan University (1990)
M.S., Geology, National Taiwan University (1994)

Submitted to the Department of Civil and Environmental Engineering
in Partial Fulfillment of the Requirements for the Degree of

MASTER OF SCIENCE IN CIVIL AND ENVIRONMENTAL ENGINEERING

at the

MASSACHUSETTS INSTITUTE OF TECHNOLOGY

September 1997

Signature of Author: _____
Department of Civil and Environmental Engineering
August 8, 1997

Certified by: _____
Patricia J. Culligan-Hensley
Assistant Professor, Department of Civil and Environmental Engineering
Thesis Supervisor

Accepted by: _____
Joseph M. Sussman
Chairman, Departmental Committee on Graduate Studies

The Use of NMR to Conduct a Microscopic Investigation of NAPL Entrapment in Porous Media

by

Rong-Tsong Horng

Submitted to the Department of Civil and Environmental Engineering
on August 8, 1997 in Partial Fulfillment of the Requirements for the Degree of
Master of Science in Civil and Environmental Engineering

ABSTRACT

Nonaqeous phase liquids (NAPLs) are major contaminants of soil and groundwater systems today. The mechanism of NAPL contamination and remediation by fluid flushing can be mainly described by the interaction of immiscible liquids in porous media. Many theoretical models have been developed to explain such interaction. However, pore scale physical observations of the interaction process itself remain scarce.

This study uses Nuclear Magnetic Resonance (NMR), which is a technique widely utilized in medical studies, to investigate NAPL remediation by hydraulic flushing from a microscopic view. Two different test types, a static test and a dynamic test, were performed in this study. To differentiate between water and the chosen NAPL contaminant oil, D_2O was used in the experiments to replace H_2O. Glass beads of equal size were used as the porous medium.

A series of 3D images at different flushing velocities were obtained during the static testing. By digitalizing these images, relationships between the flushing velocity, the shape of entrapped oil droplets and the residual oil saturation were obtained. During dynamic testing, the whole flushing process was investigated by continuous 1D spectra. The dynamic test can verify the results of the residual oil saturation obtained during the static testing program.

This study determined that NMR is a very useful tool for studying immiscible liquid interactions in porous media at the microscopic level. Further work should be done to investigate such interactions in non-uniform particles in order to approach more closely the conditons in the field.

Thesis Supervisor: Patricia J. Culligan-Hensley
Title: Assistant Professor , Department of Civil and Environmental Engineering

Acknowledgments

I would like to thank Professor Patricia J. Culligan-Hensley, Professor David Cory and Dr. Werner Mass for guiding my research. It has been a great pleasure to work in NMR laboratory in Nuclear Engineering Department. I also wish to express my gratitude to Professor C. C. Ladd, Dr. Germaine, Mr. Stephen Rudolf and Ms. Mary Eliff in Civil and Environmental Engineering, my life at MIT could not be completed without them.

I am grateful to all colleagues who have helped me. Mr. Sangkaran Ratnam and Katunori Banno supported me much in remediation experiments. I also thank Mr. Scott Packard, Yuan Chan, John Zhang, Wurong Zhang and Ms. Xiauwu Tang in Nuclear Engineering ,and Mike Kutney in Chemical Engineering, who helped me much in NMR experiments. I also pay my sincere appreciation to Mr. Issac Tseng in Nuclear Engineering and John Kaufhold in data processing laboratory, E.E. at BU, who assisted me in processing data.

Finally, I gratefully acknowledge the Taiwan Government who supported me study abroad.

Table of Contents

List of Tables

List of Figures

Chapter 1: Introduction

In recent years, much effort has been devoted to studying the mechanisms by which non-aqueous phase liquid (NAPLS) can be flushed out of soil by water (Morrow, 1979, 1991; Morrow & Songkran, 1981). If this mechanism can be well understood. the efficiency of remediating NAPL contamination by the technique of hydraulic flushing might be enhanced

Nuclear Magnetic Resonance (NMR) is a experimental technique that has been developed for decades (Fikushima, 1995). Its original purpose was to explore the composition and structure of unknown chemicals. Another use of NMR is to plroduce images of an object's interior. This application has resulted in the rapid development of NMR in the medical industry. The medical term for NMR is MRI(Magnetic Resonance Imaging) . NMR has proven a good tool not only for medical diagnosis, but also for the study of fluid transport in porous media.

Various developments have occurred in the use of NMR to investigate microscopic transport processes in a porous medium. Herald work involving the use of NMR for such a purpose began in 1979. Images depicting the distribution of fluids within porous samples were obtained by Gummerron et al(1979). Following these date, more sophisticated machines and pulse sequences enhanced the quality of NMR imagery. Hall et al. (1986,1987) obtained images of water and oil in sandstone. Chen et al. (1988) applied MRI to the study of immiscible-fluid displacement in porous media. Namdava et al. (1990) studied saturation issues in porous media during immiscible displacements using NMR imagery; their research involoved the study of dynamic displacements. Dereppe and

Moreaux (1991) used NMR to study oil-water displacements in limestone. Williams et al. (1994) obtained images of chemicals in sandstone cores during fluid flow. Recent research published by Crestana and Posadas (1995) used imaging techniques and invasion percolation models to investigate wetting front instabilities in layered soils.

This research focuses on the use of NMR to explore the mechanism of oil displacement by water in a porous medium which is modeled by glass beads. By replacing water with D_2O and using T_1 inversion, the amount and distribution of residual oil following fluid flushing and the flushing process itself have been studied in detail. Furthermore, the relationship between flushing velocity and the morphology and distribution of residual oil was also obtained by studying the NMR spectra and images.

In Chapter 2, the basic principle of NMR imagining is presented; and the NMR hardware is briefly introduced in Chapter 3. In Chapter 4, several methods in differentiating oil and water by making use of the properties of protons are discussed. Chapter 5 presents the experiments design and procedures. In Chapter 6, the mechanisms of oil entrapment during hydraulic flushing is briefly reviewed. Finally, the experimental results and conclusions are given in Chapter 7.

Chapter 2: Principle of NMR Imaging

Obtaining images by NMR requires an understanding of the theories of quantum physics. This chapter will review the basic principles of Nuclear Magnetic Resonance spectroscopy and imaging.

2.1 Nuclear Spin

In nature, most elements contain at least one isotope with a non-zero spin angular momentum, I, and a gyromagnetic ratio, r. In addition, most elements produce an associated magnetic moment u given by (Callaghan, 1995)

$$u=hrI \qquad \text{Eq. 2.1}$$

Where h is the Planck constant, and I , a quantized characteristic of the nucleus, describes the symmetry of the nuclear charge distribution. When a nuclear charge distribution is spherically symmetric, the spin I is equal to 1/2. Any interaction of spin I=1/2 is purely magnetic, and has the magnetic dipole properties described by Eq. 2.1.

Different nuclei in the periodical table have different gyromagnetic ratios(r). Hence, they produce different frequencies w_0 under certain applied magnetic fields. Examples are found in Table 2.1

The most widely studied element in both spectroscopy and imaging is ^1H because it has nearly 100% abundance in Hydrogen species, and also because it is the most sensitive

stable isotope. We also make use of hydrogen atoms in obtaining images in the experiments described in this thesis.

2-2 Zeeman Interaction

For I=1/2 nuclei, there are two values of spin along the z-direction, I_z=1/2 and I_z=-1/2. I_z=1/2 and I_z=-1/2 correspond to the nuclear magnetic moment oriented along and against the applied magnetic field. The nuclear moments are represented by cones, as show in Fig. 2.1

In an NMR experiment, the interaction between the nuclear magnetic moment and an applied external magnetic field is important. The energy of this interaction is expressed by:

$$E = -uB_0 = -hrIB_0 \qquad \text{Eq. 2.2}$$

where E is the interaction energy, and B_0 is the external magnetic field. Since I=±1/2, we can rewrite a new equation From Eq. 2. 2

$$\delta E = \frac{1}{2}hrB_0 - (-\frac{1}{2}hrB_0) = hrB_0 = hw_0 \qquad \text{Eq.2.3}$$

Where w_0 is the frequency and is equivalent to rB_0

For an ^{1}H proton, the gyromagnetic ratio r is 4,250 Hz/G. We can plot Eq. 2.3 in the form shown in Fig2.2. The magnetic intensity of the machine that was used for this research was 3T. Hence the resonance signal was 122.2MHz

2.3 Larmor Precession, FID, Block Equation and RF Pulse

Larmor precession is a rotation induced by an applied magnetic field. The motions of spin dynamics can be divided into two types:

1. The Larmar precession: This is described by Eq. 2.4, and can be viewed as a torque in classic mechanics

$$dM/dt=M*B \qquad \text{Eq. 2.4}$$

where M is the magnetic moment, B is a second applied magnetic field and t is time. M and B are usually produced by a Radio Frequency (RF) pulse.

2. Relaxation: This is shown in Fig 2.3. When the second applied magnetic field disappears, the magnetic moment will be driven back to equilibrium under the applied static field B_0. Before the system returns to equilibrium, and the bulk magnetization vector is not yet along the direction of z-axis, the magnetization will rotate about the z axis with an angular velocity w_0 given by Eq. 2.3

For a more detailed examination, the relaxation process can be divided into two components. The magnetization along the z-axis will relax towards equilibrium value M_0, and the x-y component will relax toward zero(see Fig. 2.3)

The z-axis relaxation time is called the spin-lattice relaxation time, T_1; the x-y plane relaxation time is called the spin-spin relaxation time, T_2.

The complete process of spin dynamics can be expressed by the Block Equation (Callaghan, 1995):

$$\frac{d}{dt}M(t) = rM(t)B - \frac{1}{T_1}(M_z - M_0)\hat{z} - \frac{1}{T_2}(M_x\hat{x} + M_y\hat{y}) \qquad \text{Eq. 2.5}$$

Where $\hat{X}$, $\hat{Y}$ and $\hat{Z}$ are the scalars that represent the x, y and z axis, respectively.

Thus, a magnetic field B is applied by an RF pulse to force a magnetic moment M in the x-y plane. Afterwards, this field is removed. The magnetic moment then rotates back to the z axis with angular velocity w_0. If we collect signals on the x-y plane, a damped sinusoid signal will be obtained as shown in Fig. 2.4(a). This is termed the Free Induction Decay (FID).

The angular velocity w_0 is termed larmor frequency. This frequency can be extracted from the FID by Fourier Transformation.(Fig. 2.4(b))

2.4 Magnetization Gradient, Spatial Dependency and Slice Selection

For differentiating the different slices in a sample, a measurable difference between two locations in a sample is needed. This difference is called the spatial dependency, and is approached by applying a gradient magnetic field gradient, as described by Eq. 2.6

$$B = B_0 + \frac{\partial}{\partial u} G_z \qquad \text{Eq. 2.6}$$

Where u represents the x, y and z direction, and G is the gradient magnetic field.

Under these condition, the resonance frequency will vary along the sample, as shown by Fig.2.5

After the gradient magnetic field is applied, the sample will have a spatial heterogeneity because the resonance frequency will vary over the length of the sample.

If we want to study certain parts of the sample, we can control the position of study by their specified frequencies, (Fig. 2.6 (a)). In practical terms, such control is called slice selection, and is usually achieved by a RF excitation pulse, as depicted in Fig. 2.6(b)

2.5 Gradient Echo and Spin Echo

The NMR imaging method is based on the phenomenon that magnetic field inhomogeneity will cause nuclear spins to process at different Larmor frequencies in different parts of the sample. However, there are some other factors that could affect the intensity of the applied magnetic field, such as chemical shifts and susceptibility shifts. These factors will scramble the expected Larmor frequency and result in bad images.

To delete all time-independent variations in the resonance frequencies, the gradient echo and spin echo methods have been widely used.

Before we introduce the gradient echo and the spin echo, the idea of the reciprocal space vector as depicted by Eq.2.7, needs to be introduced

$$K_i = \int r \frac{\partial}{\partial t} G_z(t)dt \; K_i = \int r \frac{\partial}{\partial t} G_z(t)dt \qquad \text{Eq.2.7}$$

Where K is the reciprocal space vector which is integrated from gradient magnetic field G.

The magnitude of K will increase with time if we apply a positive gradient magnetic field. If a negative gradient magnetic field of the same magnitude is then applied next, the value of K will return to zero because the integration of the applied magnetic field will be equal to zero. Gradient echo is composed of a RF pulse and a applied gradient, as depicted by Fig.2.7

When K is equal to zero, the net gradient magnetization will be equal to 0. Under these conditions, the signal will refocus as an echo, indicating an intensity equal to FID without the gradient magnetization field.

Spin echo can be reached simply by applying a RF pulse without a gradient magnetic field. The simplest spin echo is a Hahn echo as shown in Fig. 2.8. It shows that a 90 degree pulse along the x-axis is applied to make the bulk magnetization fall on a transverse plane. After time t, when the magnetic moment rotates w_0t, the 180 degree pulse along the y axis is applied. Then the signal will refocus at time 2t, which is known as the spin echo.

2.6 2D and 3D Images

In the processes of 2D images, the FID is sampled in the presence of a gradient, and signal points are obtained along a single line in k-space. If we impose a different G_y gradient for a constant period before sampling begins, the intercept of the K-space line and y-axis will be changed. Fig 2. 9 shows the pulse programs, gradient programs and K-space, respectively.

If the T_2 value is too short, the selective excitation methods will fail in the 2D experiment. Then 3D images should be employed. 3D images are usually obtained by a hard pulse of sufficiently short duration throughout the sample. As depicted by Fig. 2.10 , the difference between 2D and 3D images is that two phase gradients are found in 3D images.

Table 2.1
the most common used nucleus in NMR and their properties

nucleus	%abundance of nucleus in same species in nature	r(Hz/G)	W_0 (MHZ) under applied magnetic field 3T	W_0 (MHZ) under applied magnetic field 9.6T
^{1}H	99.99	4250	125	400
^{19}F	100	3995	118	376
^{31}P	100	1721	50.6	162
^{13}C	1.1	1069	31.4	100.6
^{15}N	0.37	431	12.68	40.56

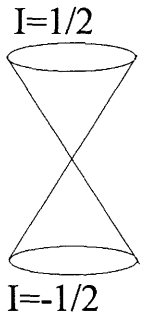

Fig 2.1 Two values of spin in a nuclei of I= 1/2

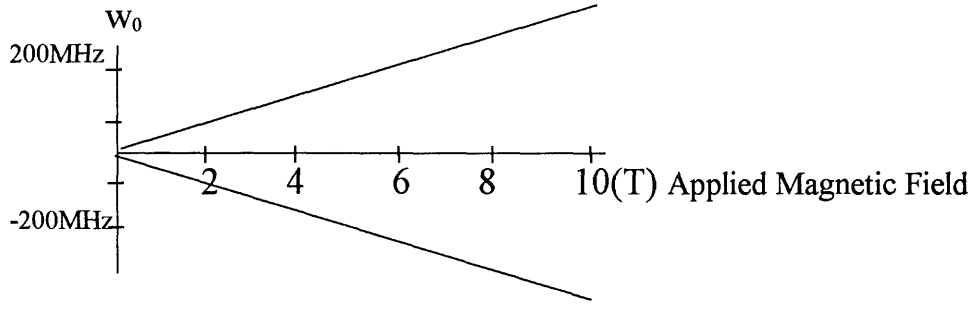

Fig.2.2 ^{1}H proton resonance frequency in the applied magnetic field

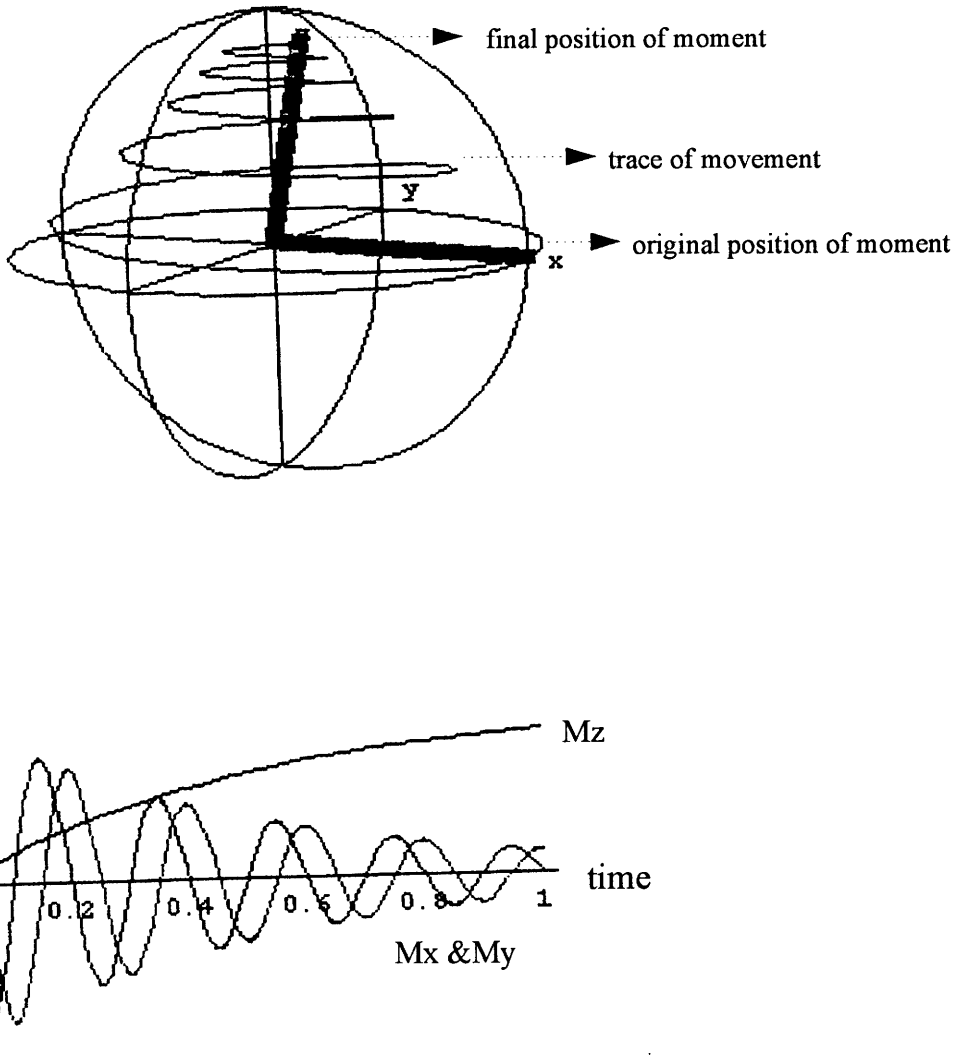

Fig 2.3 Relaxation of magnetic moment in 3D view (upper) and its Relaxation of magnetic moment shown as two components (below)

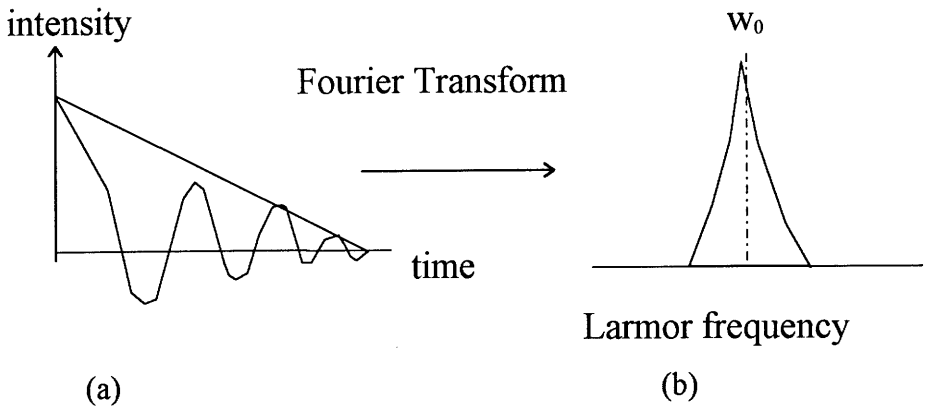

Fig. 2.4 Fourier transformation of FID

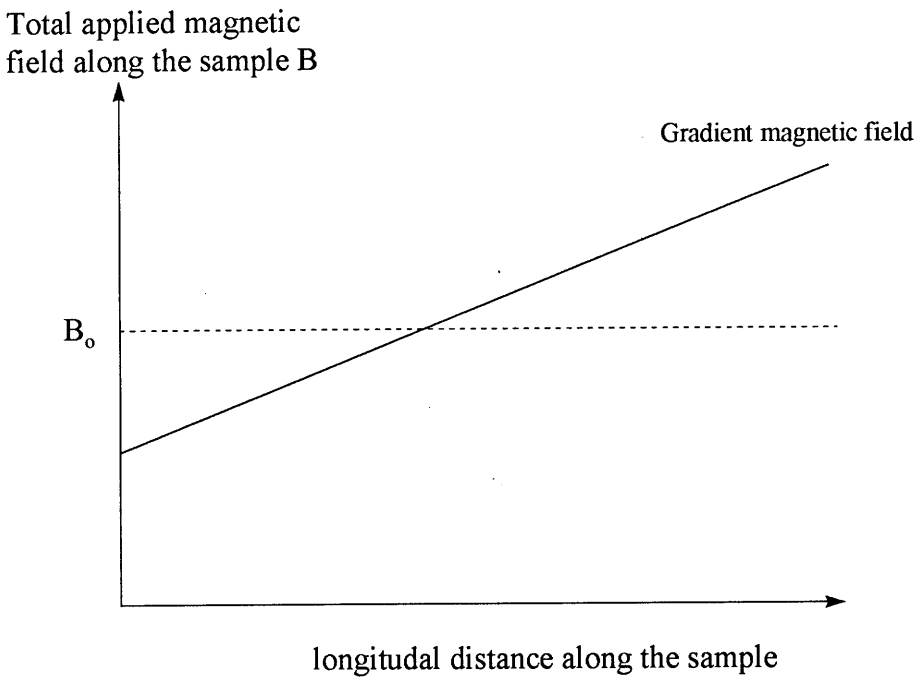

Fig. 2.5 The gradient field distribution in the sample

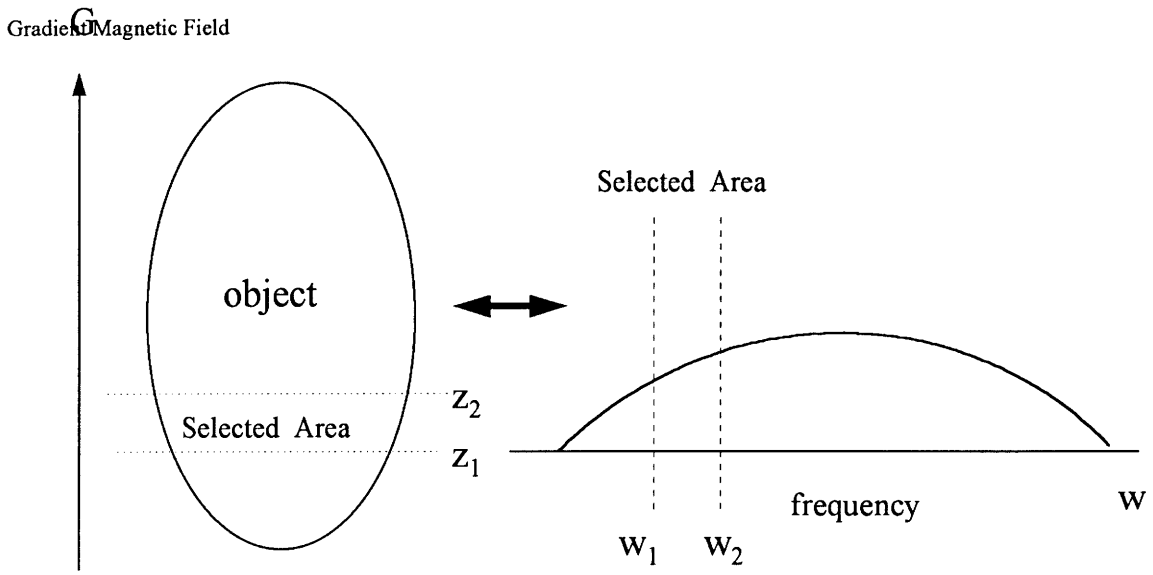

(a)

Fig. 2.6 (a): Different parts of an object can be identified by gradient magnetization.

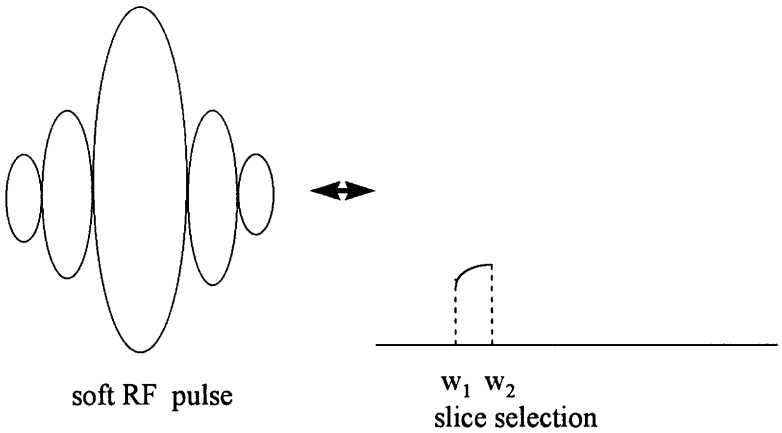

(b)

Fig. 2.6 (b): Through soft RF pulse, the specified slice can be obtained in images.

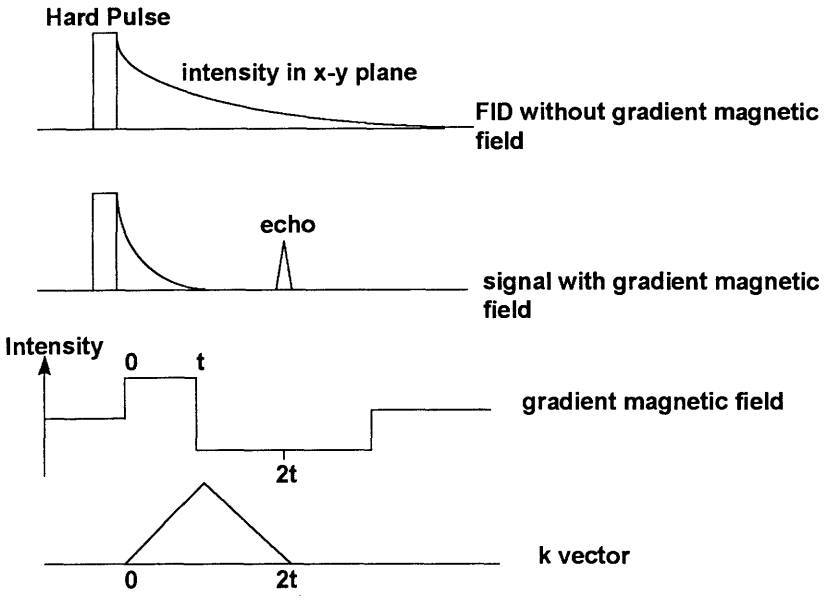

Fig. 2.7 (a) FID without gradient magnetization field (b) Gradient echo: signal with gradient magnetic field and k vector

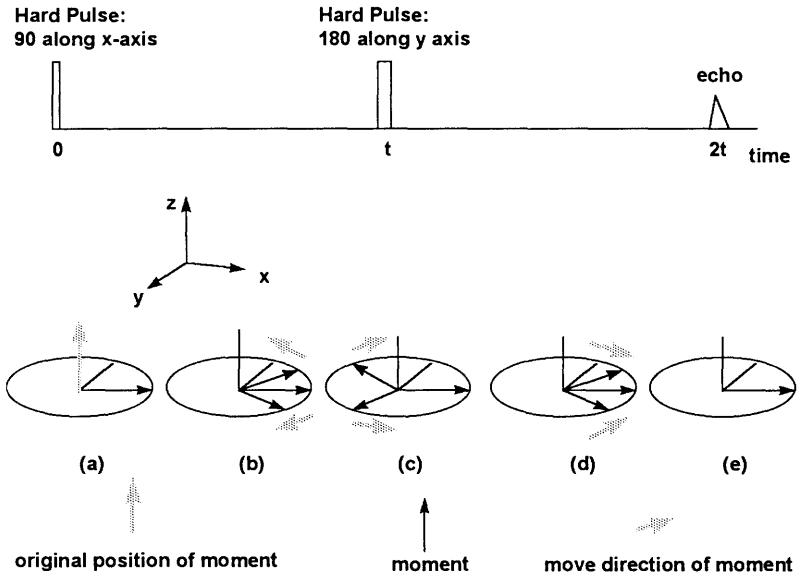

Fig. 2.8 Spin echo pulse showing the evolution of the magnetization (a) From Iz to Iy by 90x (b) Evolution components : $Iy*\cos(\delta w_0 t) + Ix*\sin(\delta w_0 t)$ (c) Following the 180y pulse at time t, components becomes $Iy*\cos(\delta w_0 t) - Ix*\sin(\delta w_0 t)$ (d) to (e) at time 2t, components evolve to Iy

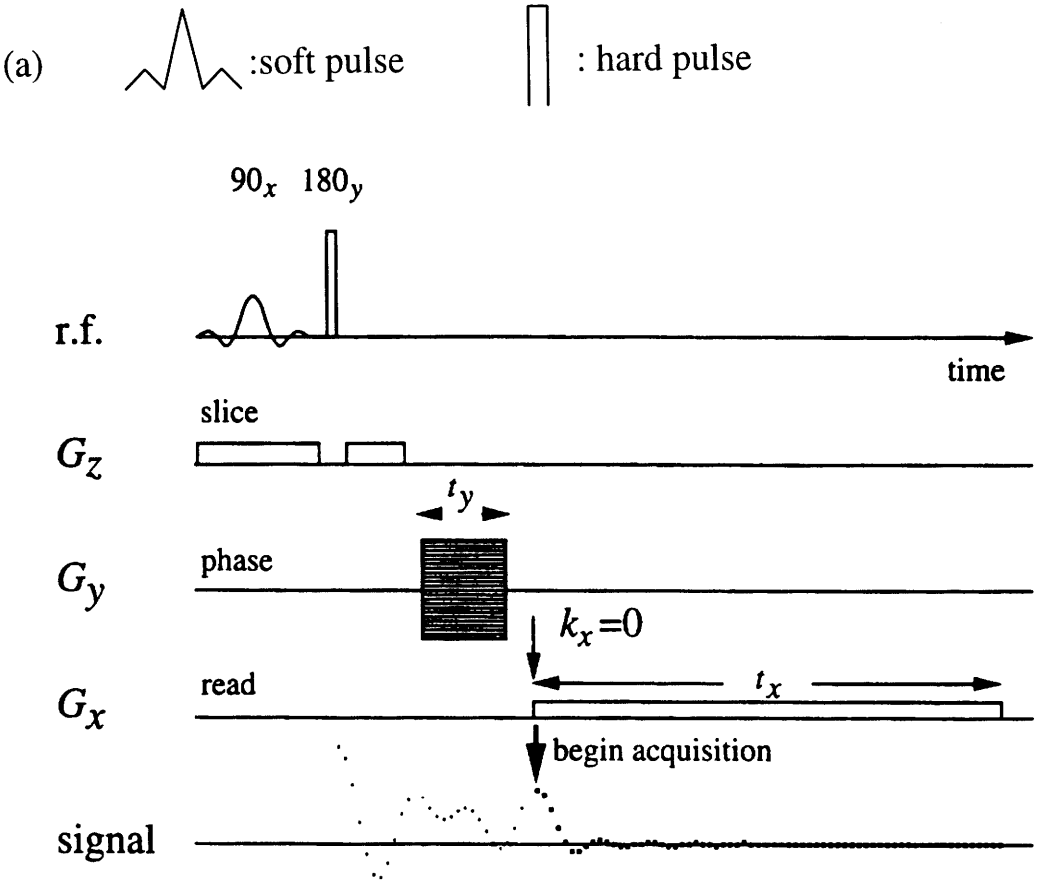

Fig 2. 9(Paul T. Callaghan, P.125) (a) pulse and gradient program for 2D images (b) k-space in 2D images

(a)

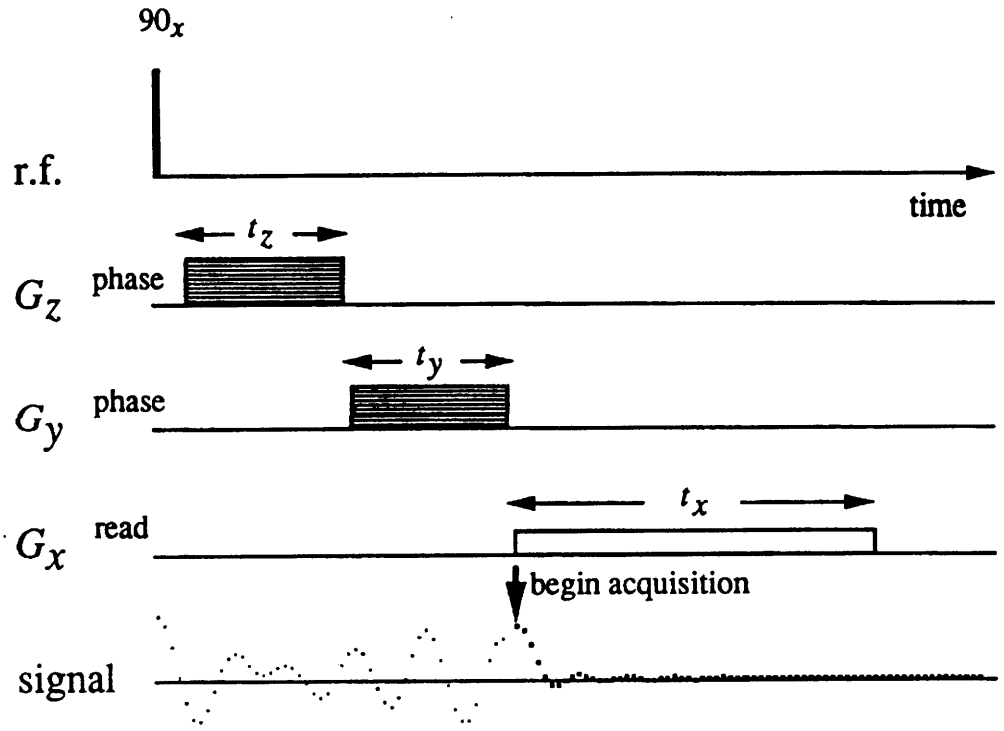

(b)

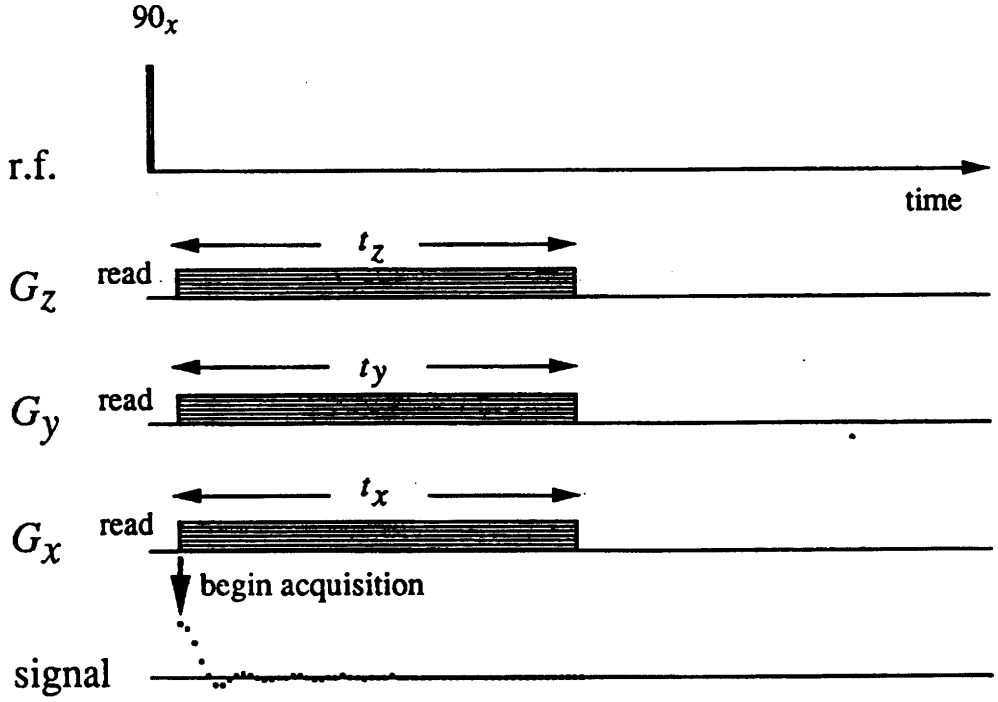

Fig 2.10(Paul T. Callaghan, P.131)Pulse and gradient sequence for 3D images.(a) FI pulse sequence (b) PR pulse sequence

Chapter 3: The NMR Hardware

According to the basic principles of NMR imaging, which are described in Chapter 2, there are three important parts necessary to the process of taking images: namely, the application of the static magnetic field B_0, the applied magnetic field B_1, and the gradient magnetic field G. All the magnetic fields are achieved individually by the specific instruments described in the following sections.

3-1 Static Magnetic Field- Magnet Machine

The strength of the static magnetic field is far larger than that of the gradient magnetic field. Depending on individual necessity, the strength of a static magnetic field can vary from several Tesla to tens of Tesla.

In the MIT magnet laboratory, the entire static magnetic field is derived from magnet machines which were made by Brunker Company. The machine used in the experiment described in this thesis was a three Tesla machine (Fig. 3.1). Therefore, it produced 122.19 Mhz when a ^1H proton is used. (see Fig. 2.2)

Due to the superconducting devices in the magnet machine, it has to be maintained in a low temperature environment. Thus, periodically refilling the machine with Nitrogen at specified intervals is very important in order to prevent breakdown of the machine.

3-2 Applied Magnetic Field- RF Coil

The applied magnetic field is induced by an RF coil. An RF coil can produce an RF pulse and a magnetic field is then produced at the same time.

The RF coil plays an important role in taking images because it not only produces the RF pulse, but it also collects signals from the sample. The homogenous magnetic field produced by the RF coil is one of the decisive factors in obtaining a good image. Therefore, the quality of the RF coil in the NMR hardware is very important.

3-3 Gradient Magnetic Field

In order to specify a measurement position in a three dimensional object, a gradient magnetic field in the x, y and z directions is necessary.

The x, y, and z gradient magnetic fields are executed by wires outside the RF coil, and controlled by an amplifier.

Fig. 3.2 provides a schematic example of the structure of an RF coil and gradient magnetic wire. The RF coil and gradient magnetic wire are put into the magnet machine which exerts the static magnetic field, Figure 3.3.

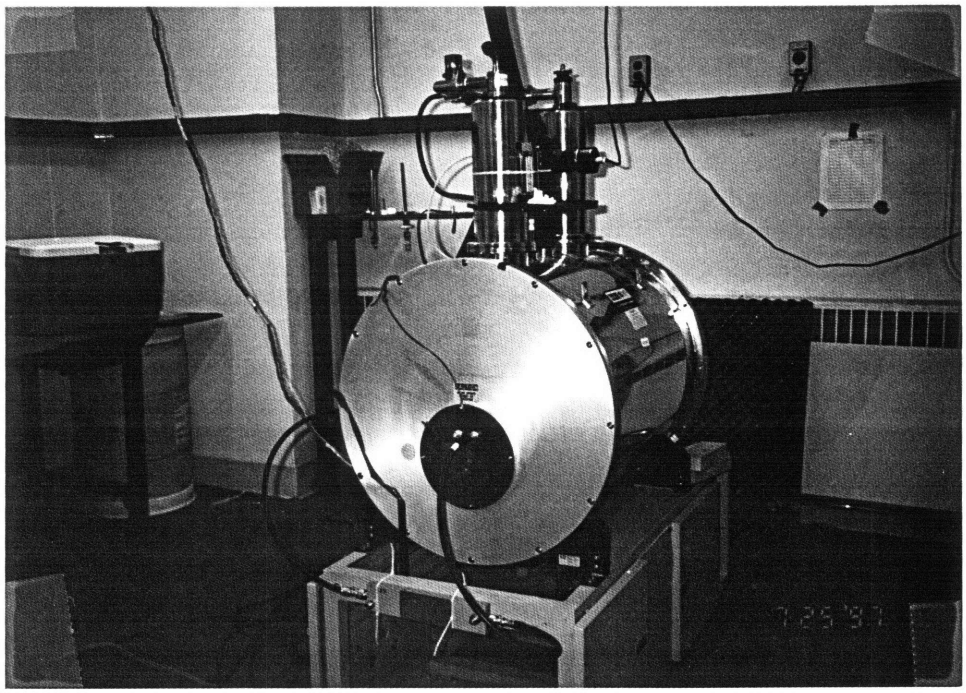

Fig. 3.1 3T NMR machine

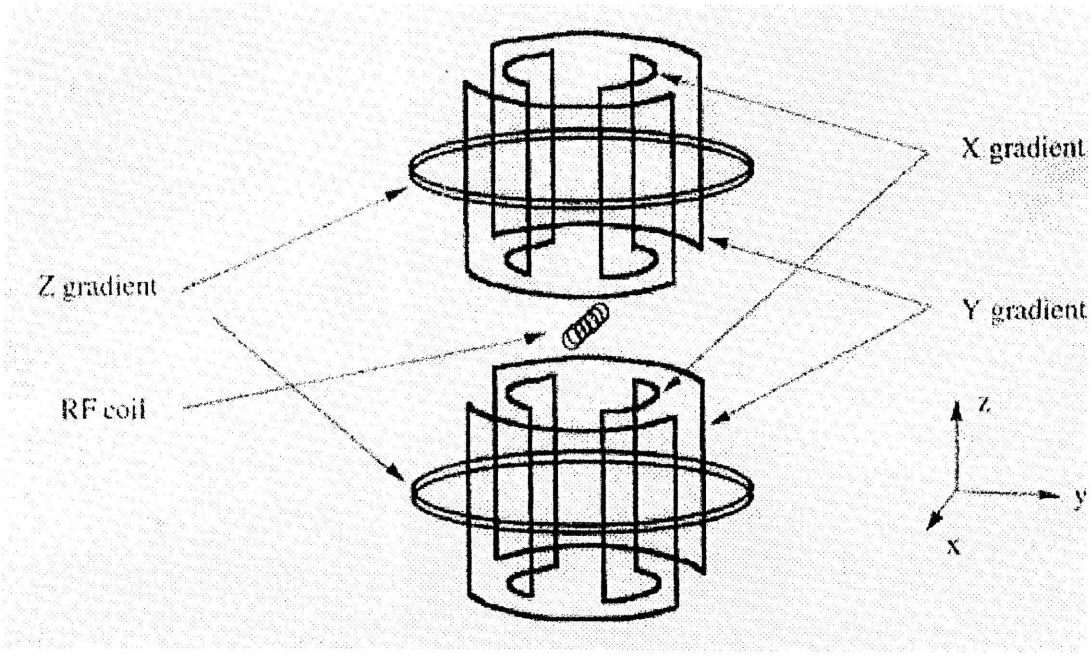

Fig. 3.2 The structure of RF coil and gradient

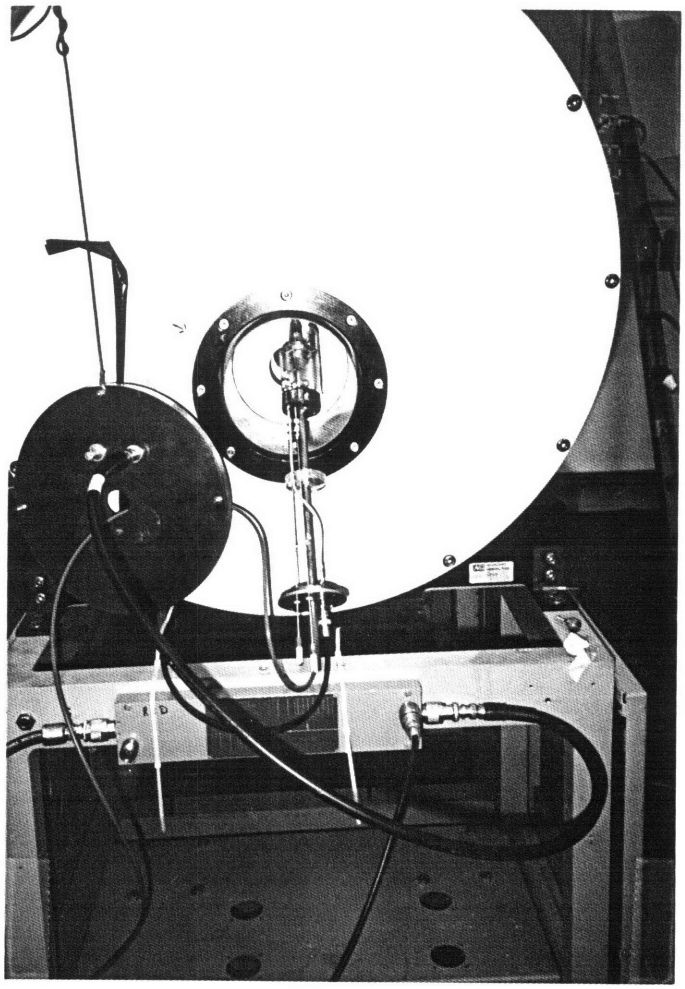

Fig. 3.3 Sample, RF coil, gradient magnetic field and 3T machine. The sample is put into RF coil, then the RF coil is put into the case of the gradient magnetic wire which is placed in the 3T machine

Chapter 4: Differentiating Oil and Water Using the NMR Process

Both water and oil contain ^1H protons, which will show signal in the NMR process. In order to differentiate between the ^1H protons in oil and water, certain methods were tried in this study.

4-1 T_1 Inversion

When we force the magnetic moment from +z to -z direction, the magnetic moment will return back to +z direction. This process has been described in Chapter 2, and it can be expressed by the equation:

$$Mz = 1 - 2e^{\frac{-t}{T_1}} \qquad \text{Eq. 4.1}$$

Oil and water have different T_1 inversion times. Through the T_1 inversion test, we can construct a figure (Fig. 4.1) to describe the inversion process. Fig. 4.1 shows that the signal for oil will disappear in z direction at t=350ms while the water will still have a magnetic component in -z direction at t=350ms. At t=900ms, the situation will change; in other words, the oil will display a signal, while the water signal will disappear.

If we collect a measurement when one component disappears and the other one still has signal, we can hide one component and show the other one in the image. Hence, it should be possible to differentiate oil and water from the recorded image using this

method. Fig. 4.2 shows an image from T_1 inversion. The T_1 inversion is controlled to hide water protons and thus highlight oil. Although this is a good method to differentiate oil and water, it is hard to apply this technique to a study in porous media. Because oil and water are trapped unevenly in small pores between the solid phase in the porous media, the signals from both are too faint to differentiate. (see Fig. 4.3)

4-2 Chemical shift

Since the chemical structures of oil and water are different, the ^1H protons in each structure will be bound by different molecular forces. Hence the protons will produce a frequency shift between the different structures. This shift is called a chemical shift and is described by the following equation.

$$\omega=\gamma(B_0+\Delta B) \qquad \text{Eq. 4.2}$$

where ΔB is the induced frequency shift, which has a magnitude that is proportional to static magnetic field B_0. In our experiment, we used a 3T machine to obtain images. The static magnetic field produced by this machine is not large enough to separate the ^1H protons in oil and water by the magnitude of ΔB. Thus, the chemical shift method could not be applied in the experiments reported here.

4-3 D_2O

D_2O is composed of ^2H, which has a different frequency in comparison to ^1H. If we replace water with D_2O in the experiment, then the signal from the sample will disappear because we can only collect signals in a range that fits ^1H proton.

This method proves to be successful in testing, and was therefore adopted for the study. Fig. 4.4(a) shows an image of oil and glassbeads in a tube. After flushing D_2O through the tube, we find that we can easily differentiate D_2O from oil. As shown in Fig. 4.4(b), the D_2O is darker than oil due to the fact that it produces no signal.

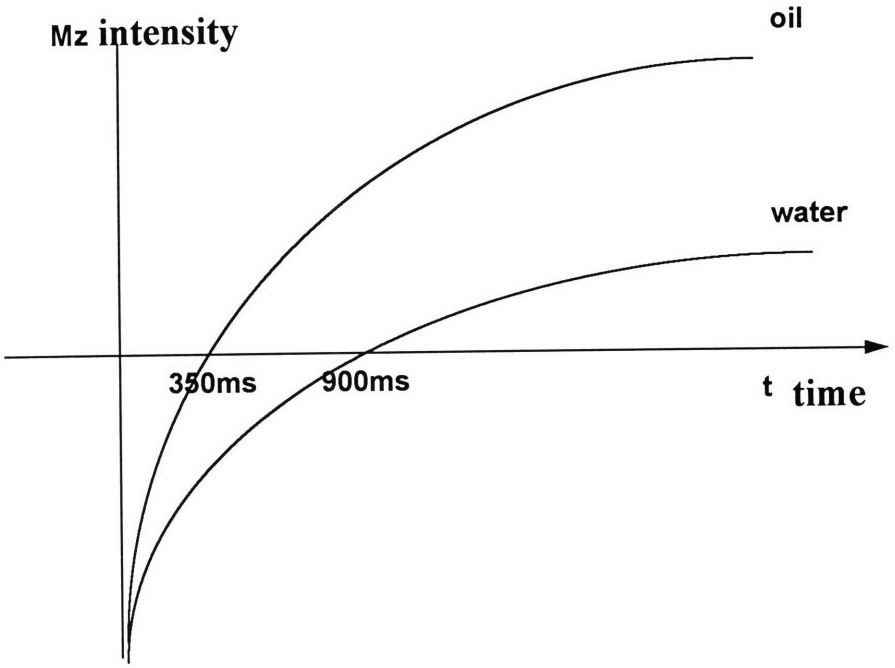

Fig. 4.1 T_1 Inversion test of oil and water

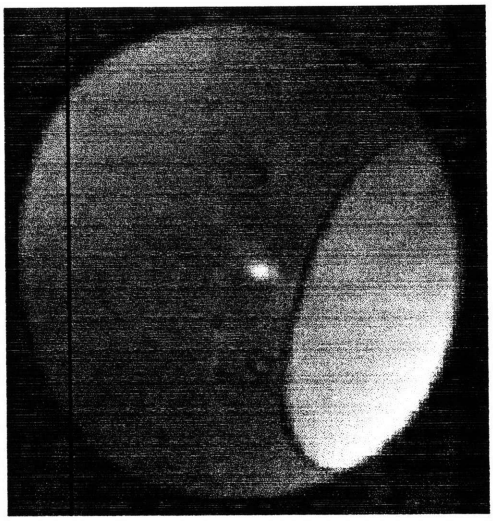

Fig. 4.2 Image of water and oil by T_1 Inversion (the light part is oil)

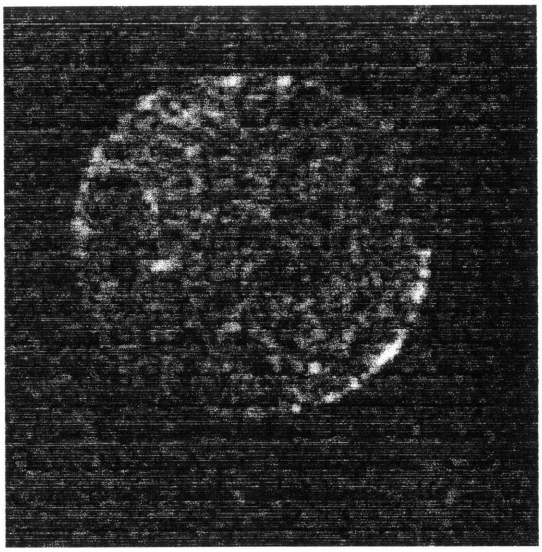

Fig. 4.3 The image of soil, oil and water in a tube

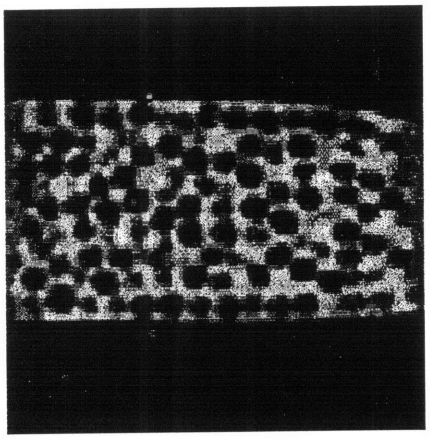

Fig. 4.4 (a) Image of oil and glass beads in a tube

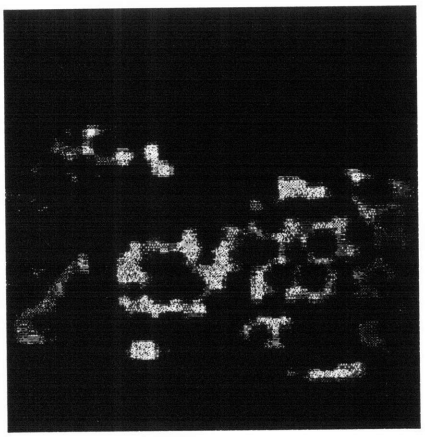

Fig. 4.4 (b) After flushing D_2O into the setup described by Fig. 4.4 (a)

Chapter 5: Experimental Design and Procedure

For many years, researchers have believed that there is a relationship between the water-flushing velocity and quantity of leftover oil during oil recovery by the technique of hydraulic flushing (Stegemeier, 1976; Ratnam, 1996) The experiment described here was designed to study this relationship.

5-1 Experiment Devices

All experiments were conducted in a tube, Fig. 5.1, which initially contained glass beads and oil and was subsequently flushed by D_2O. In order to produce a homogeneous pistol flow throughout the tube, ten layers of filter paper were placed in the inlet where the D_2O was introduced.

The inlet part of the tube was connected to a pump, which was used to control the speed of D_2O flushing.

5-2 Experimental Procedure

Air bubbles can disturb the homogeneity of the magnetic field inside the tube and can therefore result in a bad image. Hence, keeping air bubbles out of the sample is very important. The best way to prevent air bubbles from being trapped between glass beads is to place the oil in the tube first, then slowly introduce the glass beads. To control the packing of the glass beads, the porosity of the porous medium was set at 0.4 for each test in the study.

1. Static Test

After sample preparation, the tube was flushed with one pore volume (1PV) of D_2O at different speeds. This flushing process expelled oil. However, following flushing, some oil still remained trapped behind the flushing front in the pore space between the glass beads. By halting the flushing after 1PV of D_2O was introduced, no more oil could be expelled from the tube. At this stage, the tube was sealed at both ends and placed horizontally in the NMR machine to obtain images.

During each experiment, sixteen images were taken within a length of 1.5 cm. These images allowed us to see the leftover oil in the tube, which showed up as white (see Fig. 4.4). Furthermore, the images could be digitized using Matlab and the volume of residual oil following flushing could be calculated from the digitized image.

2. Dynamic Test

In order to study in more detail the hydraulic flushing process itself and to verify the results obtained in the static experiments, dynamic testing was also performed.

During a dynamic test, the data were acquired every 200ms while the flushing process was on-going, again in a horizontal direction. At each time interval, a one dimension signal was taken along the length of the tube. Before the D_2O was flushed in, the signal that was produced by the oil was evenly distributed in every part of the tube. The signal then decayed with time as the D_2O moved in and replaced the oil. From the shift of the boundary of signal decay, we can trace the D_2O front. If we calculate the ratio of signal intensity before and after flushing, we can also obtain the percentage of trapped oil. After 1PV of flushing, this value should be the same as the value obtained from the static experiment described above.

In the dynamic experiment, the flushing velocity must be held constant. To meet this criterion, the syringe pump Varian 8500 (Fig. 5.2) with motion controls was used in this experiment rather than the general motor pump which was used in the static experiment.

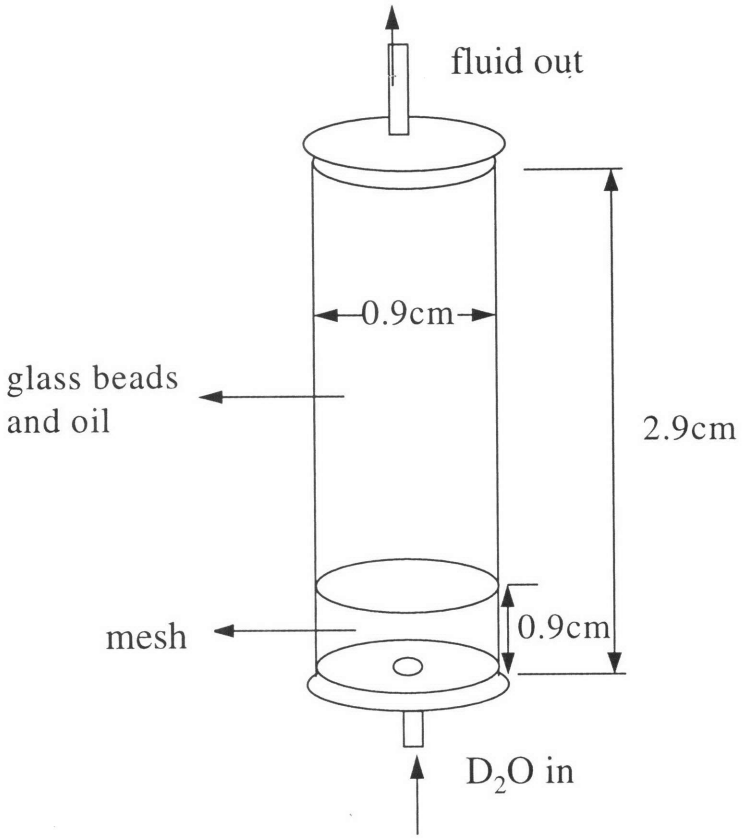

Fig. 5.1 tube with glass beads and oil. After flushing, the tube was sealed and placed into the 3T machine

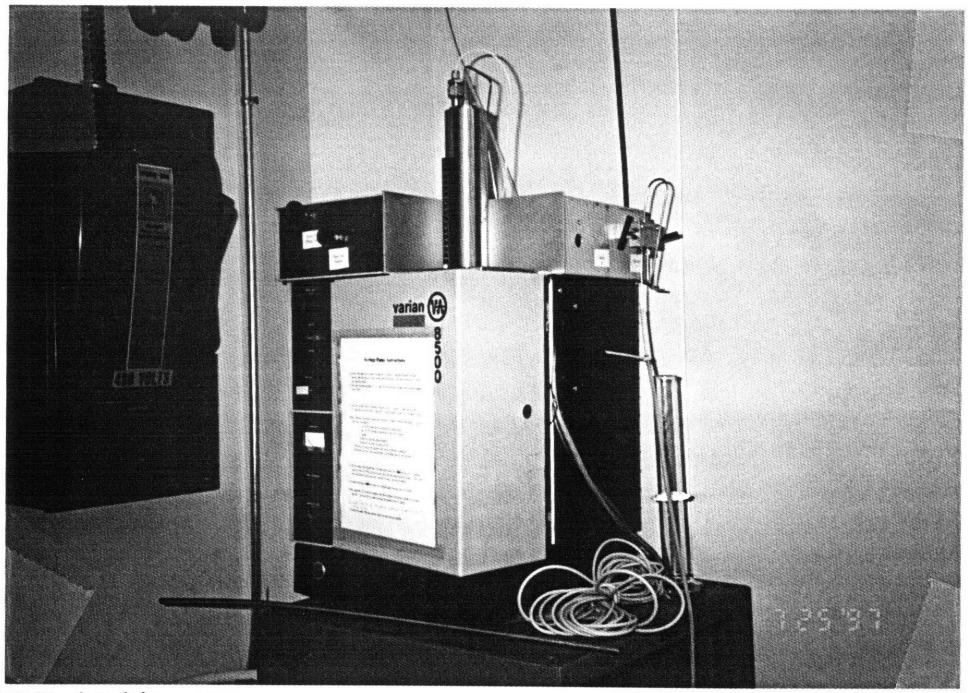

Fig. 5.2 Peristaltic pump

Chapter 6: Mechanism of Oil Entrapment

6.1. Oil Entrapment Mechanism

Mace and Wilson (1991) proposed 'snap-off' and 'by-passing' as two mechanisms for NAPL entrapment during fluid flushing in saturated water-wet porous media (Fig. 6.1). In general, the factors that affect the mechanism of entrapment include: geometry of the pore network; fluid-fluid properties such as interfacial tension, density difference, viscosity ratio, and phase behavior; fluid-rock interfacial properties which determine wetting behavior; and the body force and pressure gradient (Ratnam, 1996)

A model for NAPL entrapment can be derived by equations that describe the static force balance for the NAPL and water in a porous medium. Two major pressures, the supplementary pressure, P_s, and the capillary pressure, P_c, are dominant in the system.

The supplementary pressure is induced by buoyancy forces and viscous pressure forces (Wardlaw and McKellar, 1985; Mayer and Miller, 1992).

The contribution that buoyancy force supplies in supplementary pressure, $P_{s(b)}$ is computed over the length of a trailing finger of NAPL during aqueous phase displacement (see Fig 6.2), and is given by:

$$p_{s(b)} = -g(\rho_a - \rho_n)l \qquad \text{Eq. 6.1}$$

where;

ρ_a	is the density of the aqueous phase
ρ_n	is the density of the non-aqueous phase (LNAPL)
g	is the gravity vector
l	is the length of the trailing finger in the direction of g

Viscous force in supplementary pressure, $P_{s(b)}$, is computed over the length of the trailing finger from Darcy's Law as:

$$p_{s(v)} = \frac{v_a u_a l}{k} \qquad \text{Eq. 6.2}$$

where;

v_a	is the aqueous phase Darcy velocity
u_a	is the aqueous phase dynamic viscosity
l	is the length of the trailing finger measured in the direction of v_a
k	is the intrinsic permeability of the porous medium

The total supplementary pressure is supplied by a combination of buoyancy forces and viscous pressure forces. When the two component both act in the same direction to overcome the forces promoting entrapment, e.g. in the case of the upward displacement of oil by water, $P_{s(b)}$ and $P_{s(v)}$ can be combined to give

$$p_s = p_{s(b)} + p_{s(v)} = \left[\frac{v_a u_a l}{k} - g(\rho_a - \rho_n)\right] l \qquad \text{Eq. 6.3}$$

The supplementary pressure is balanced by capillary pressures, which are induced by the differential pressure across the interface of two fluid phases as given below(Dullien, 1992; Melrose and Brander, 1974):

$$p_c = p_n - p_a = \frac{(2\sigma_{na}\cos\theta)}{r_m} p_c = p_n - p_a = \frac{(2\sigma_{na}\cos\theta)}{r_m}$$

Eq. 6.4

where;

P_n	pressure in non-wetting (NAPL) phase (e.g. oil)
P_a	pressure in wetting (aqueous) phase (e.g. water)
σ_{na}	is the interfacial tension between the two phases
	is the contact angle

r_m is the ratio between a microscopic characteristic length for a porous medium and the limiting curvature for imbibition at the fluid phase interface

The maximum length (l_{max}) of a trailing finger that will disconnect to form an isolated blob can be derived by balancing the pressures, vis:

$$l_{\max} = \frac{2}{r_m}\left[\frac{v_a u_a}{k\sigma_{na}} + \frac{g(\rho_a - \rho_n)}{\sigma_{na}}\right]^{-1} \qquad \text{Eq. 6.5}$$

The ratio of viscous pressure forces to capillary pressure forces is often described by the dimentionless capillary number (Forster, 1973).

$$C_a = \frac{\mu_a u_a}{\sigma_{na}} \qquad \text{Eq. 6.6}$$

Likewise, the ratio of buoyancy pressure forces to capillary pressure forces is usually described by the dimentionless Bond Number (Forster, 1973):

$$B_0 = \frac{g(\rho_a - \rho_n) r_m}{\sigma_{na}} \qquad \text{Eq. 6.7}$$

6.2. Study of oil entrapment

Research about entrapment and mobilization of oil in porous media was heralded by the petroleum industry, in order to meet the need of improving the efficiency of oil recovery from petroleum bearing strata (Stegemeier, 1997; Morrow, 1991). Ng et al (1978), Morrow (1979), and Marle (1991) divided the oil recovery process into three stages and investigated their respective characteristics with different flushing materials. Many studies have been devoted to enhancing the oil recovery through the use of a wide

variety of techniques(Buckley, 1991). The results of this work are meaningful for environment remediation work: methods similar to those used by the petroleum industry for oil recovery can be applied to flushing out non-aqueous phase contaminants in polluted aquifers.

Most previous studies presented in the literature concentrated on the influence of the Capillary Number (see Eq. 6.6) on immiscible fluid flow in porous media (Morrow, 1979; Morrow and Songkran, 1981). In general, these studies neglected the influence of gravitational forces on immiscible fluid flow. Recently, Ratnam, et al. (1996a) used a geotechnical centrifuge to study the influence of gravitational forces on oil recovery during hydraulic flushing under realistic field scale conditions.

Unlike much of the research reported in the literature, which has investigated the mechanism of oil entrapment from the macroscopic view, the work reported here focused on a microscopic study of oil entrapment during hydraulic flushing through the use of NMR technology.

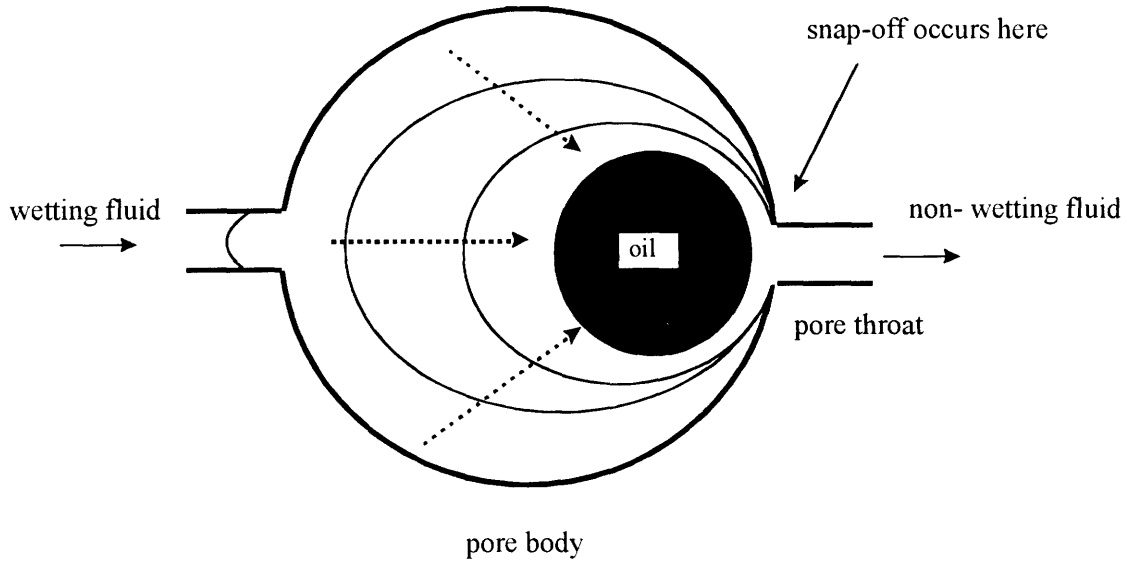

(a) Snap-off in a water wet, high aspect ratio pore

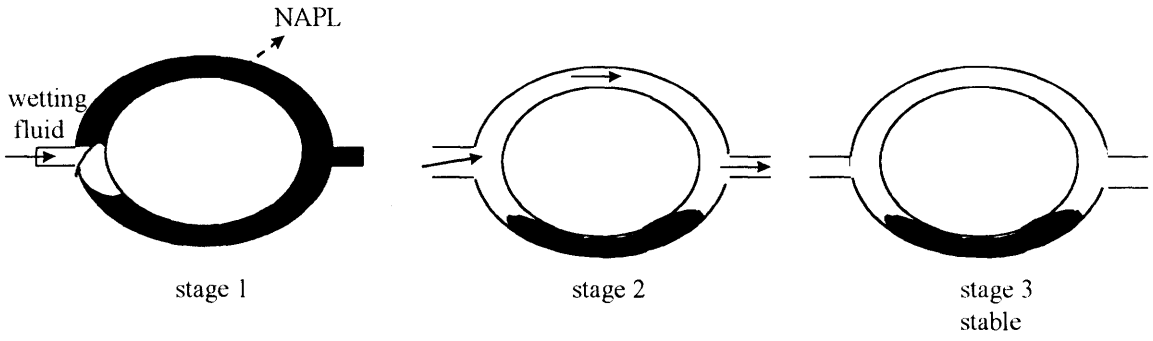

(b) trapping via by-passing

Fig 6.1 Oil entrapment mechanisms (revised from Mace & Wilson, 1991)

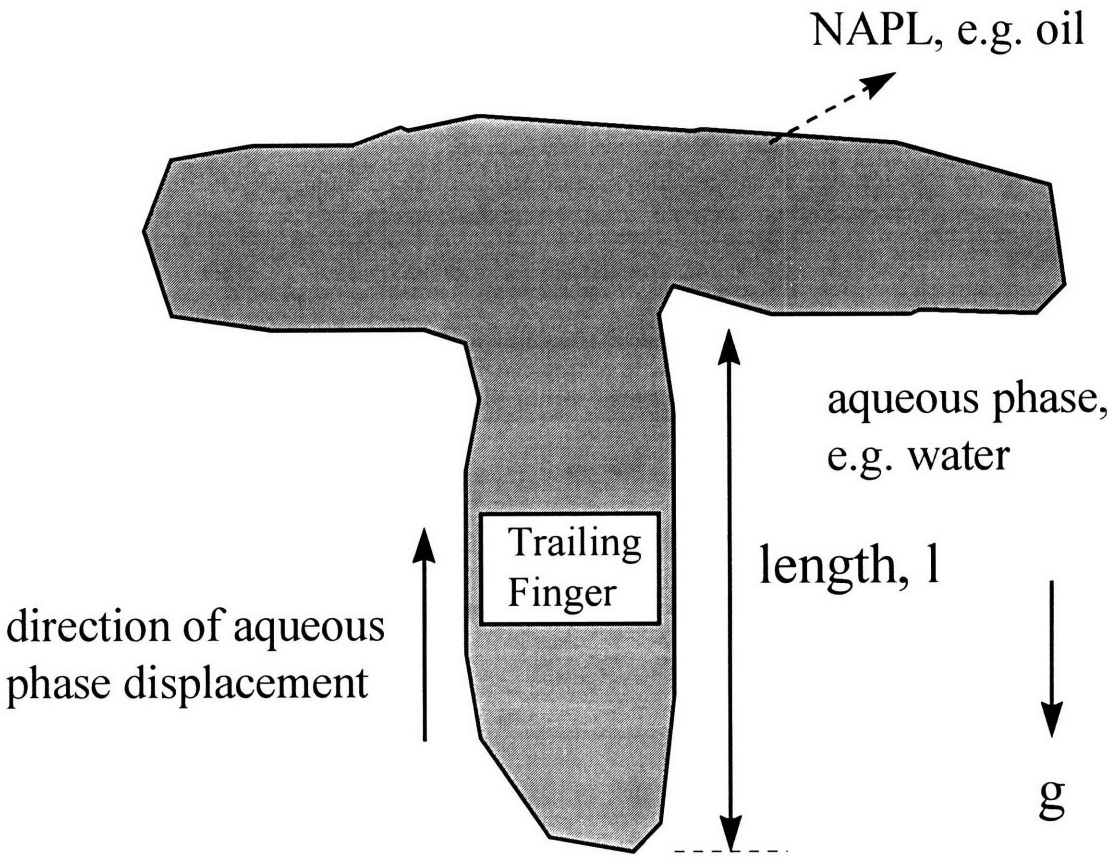

Fig. 6.2 The trailing finger

Chapter 7: Experimental Results and Conclusions

7.1 Static Experiment

In the static experiment, the imaging window was about 15mm long and was located in the center of the tube(Fig. 7.1). In these tests, four different flushing speeds were used: namely V_1= 0.05 mm/sec, V_2= 0.1 mm/sec, V_3= 0.5 mm/sec and V_4= 1 mm/sec. These flushing speeds correspond to pore fluid velocities of 0.125mm/sec, 0.25mm/sec 1.25mm/sec and 2.5mm/sec respectively, assuming a volume porosity for the glass bead medium of n= 0.4 .

After collecting NMR data using the equipment and procedures described in previous chapters, they were processed using Matlab. The images that were produced by this processing are shown in Fig. 7.2(a)-(d). By selecting a specific threshold of image intensity to define the presence of oil, the oil droplets can be digitized as revealed in Fig 7.3(a)-(d).

In all, sixteen slices were taken over the length of the excited scope window as illustrated by Fig.7.2 and Fig 7.3. Each slice is around 0.9mm. After calculating and comparing data from different slices and between tests conducted at different flushing velocities, the relationships between flushing velocity, entrapped oil droplet volume and the shape of the entrapped oil droplets can be found.

The experimental results show that there is an inverse relationship between droplet shape and flushing velocity. As Table 7.1 reveals, the average volume of an entrapped droplet decreases as the flushing velocity increases. The average droplet length and maximum droplet width also decrease as flushing velocity increases, which can be identified from Tables 7.2 , 7.3 and 7.4, and also from Fig 7.4 and Fig 7.5.

After choosing the threshold and digitizing the oil droplets in each section, we can calculate the leftover oil following 1 PV of flushing. Table 7.5 demonstrates that the faster the flushing velocity, the less oil is leftover. Fig.7.6 compares these data with data from experiments conducted by Ratnam et al (1996b) and Morrow (1981), the data obtained from the static tests were higher than those reported by Ratnam et. al. and Morrow and Songkran, however, both show the same trend. The higher leftover volume observed from the results of the experiments reported here might have been caused by the presence of larger pore spaces in the uniform glass beads used in these experiments.

From the above findings, it is apparent that higher flushing velocities can produce higher momentum, resulting in the breakdown of oil into smaller droplets. This means that a higher percentage of oil can be recovered under higher flushing velocities. However, that the remaining oil is distributed in smaller droplets might make subsequent remediation by tertiary flushing methods more problematic.

7.2 Dynamic Experiment

The dynamic experiments used the longer tube (6cm) and wider observation window (18mm) than the static experiments. During the dynamic experiments, data on the flushing process were acquired every 200ms as integrated spectra. Before the D_2O enters the excited scope window, the spectrum is supposed to be uniform if the RF pulse from RF coil is homogeneous. However, for the experiments reported here, the original spectrum was not uniform due to inhomogenity of RF coil, as Fig 7.7 shows. Through massaging the data, we can get a uniform signal by timing corrected factors into the original data sets as illustrated in Fig 7.8. If we time the same corrected factors into every

subsequent data set , then the effects of inhomogenity of the RF coil can be ruled out and the flushing process can be observed from the corrected signal decay.

In Fig. 7.9(a) and Fig. 7.9(b), the flushing process is shown as a series of spectra. Before the D_2O is flushed in, all signals originated from uniformly distributed oil in the glass medium and form a square shape spectrum; although the spectrum exhibits some fluctuations due to the presence of the glass beads which produced no signal. When the D_2O arrives at the observation window, the oil is flushed out and signals decay from the D_2O inlet of the observation window. After several pore volume of D_2O have flushed through the tube, the signal stabilizes, suggesting that no further oil is being extracted by the flushing process.

The spectrum area can be integrated at a specified time to give an index of oil content since all signals come from the oil protons. From this integration, we can see the change of oil content in the tube during the flushing process. Fig.7.10 shows the decreasing process of oil signals as time progresses. The integral signal decreases rapidly while D_2O flushes through the tube and forces oil out. After D_2O flows through the tube completely, the integral signal remains constant. Such constancy means that no more oil will be flushed out as the D_2O continues to flush in. Thus, the remnant signal comes from oil that is trapped in the pore spaces between the solid particles. Comparing the remnant signal intensity with the maximum signal intensity before flushing, we can plot a chart that shows the leftover percentage of oil under flushing(Fig. 7.11).

The leftover percentage is inversely proportional to the flushing velocities, being 25% and 15% in relation to the velocity of 0.6mm/sec and 3mm/sec, respectively. The value obtained from the dynamic experiment is close to, and verifies, the value we

obtained in the static experiment, see Table 7.5. In Fig. 7.11, the fluctuation of the spectra before flushing is due to the instability of the system. This instability should be removed in advanced experiments.

7.3 Conclusions

Four static and two dynamic experiments were carried out to investigate the microscopic relationships between the flushing velocity and the residual oil saturation and entrapped oil morphology during the displacement of oil by water in a uniform porous medium.

From the static testing, an inverse relationship between oil morphology and flushing velocity was obtained from processed NMR images. The faster the flushing velocity, the smaller the dimension of the entrapped oil droplets and the lower the residual oil saturation. Hence, high flushing velocity can result in better oil recovery.

Dynamic experiments were performed to examine the actual flushing process by one dimensional spectra. Data were collected every 200ms and the flushing process was studied by a series of spectra. Again, it was noted that the faster the flushing velocity, the less oil is left behind the flushing front. Such a finding supports the results of static experiment.

Because the sample used to take images in NMR should not have any remnant magnetism, this experiment used uniform glass beads instead of soil particles found in nature. Further studies should focus on nonuniform particles, in order for the results to represent more realistically those conditions found in the natural environment.

Table 7.1 Entrapped oil droplet numbers categorized by volume and velocity

	Greater than 5mm^3	5~4 mm^3	4~3 mm^3	3~2 mm^3	2~1 mm^3	1~0.5 mm^3	0.5~0.1 mm^3
V_1	3	1	0	4	12	8	6
V_2	1	1	1	5	7	8	6
V_3	0	0	0	0	8	14	20
V_4	0	0	0	1	5	14	21

Table 7.2 Length distribution of entrapped oil(1)

	longer than 0.94mm	Shorter than 0.94mm	total number of entrapped blobs
V_1	34	92	126
V_2	29	84	113
V_3	42	189	231
V_4	41	165	206

Table 7.3 Length distribution of entrapped oil(2)

	7.52~ 6.58mm	6.58~ 5.64mm	5.64~ 4.7mm	4.7~ 3.76mm	3.76~ 2.82mm	2.82~ 1.88mm	1.88~ 0.94mm
V_1	1	0	2	2	8	8	13
V_2	0	0	1	2	2	15	9
V_3	0	0	0	0	3	9	30
V_4	0	0	0	0	3	8	30

Table 7.4 Greatest width of entrapped oil droplets (> 1mm)

	No. of droplet
V_1	22
V_2	12
V_3	8
V_4	7

Table 7.5 Volume of Entrapped Oil (V_0=0.258c.c.)

	Ca* 10^6	Leftover(Volume)	Leftover(Percentage)
V_1	5.55	0.064 c.c.	24.8%
V_2	11.11	0.057 c.c.	22.1%
V_3	55.55	0.045 c.c.	17.4%
V_4	111.1	0.034 c.c.	13.2%

PS: $C_a = \frac{\mu_a u_a}{\sigma_{na}}$, viscosity ($\mu$) = $1.124*10^{-3}$, surface tension (σ) = 0.0253 N/m

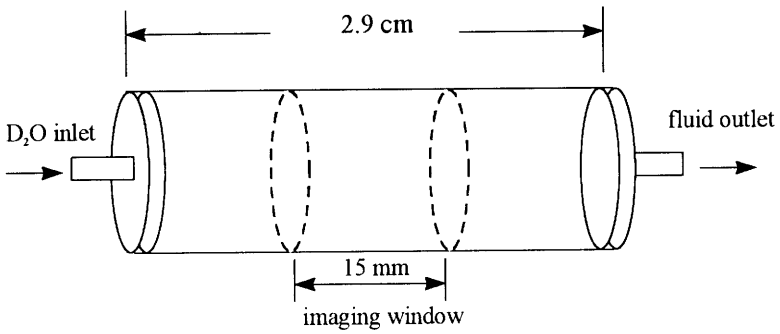

Fig. 7.1 imagining window of static test

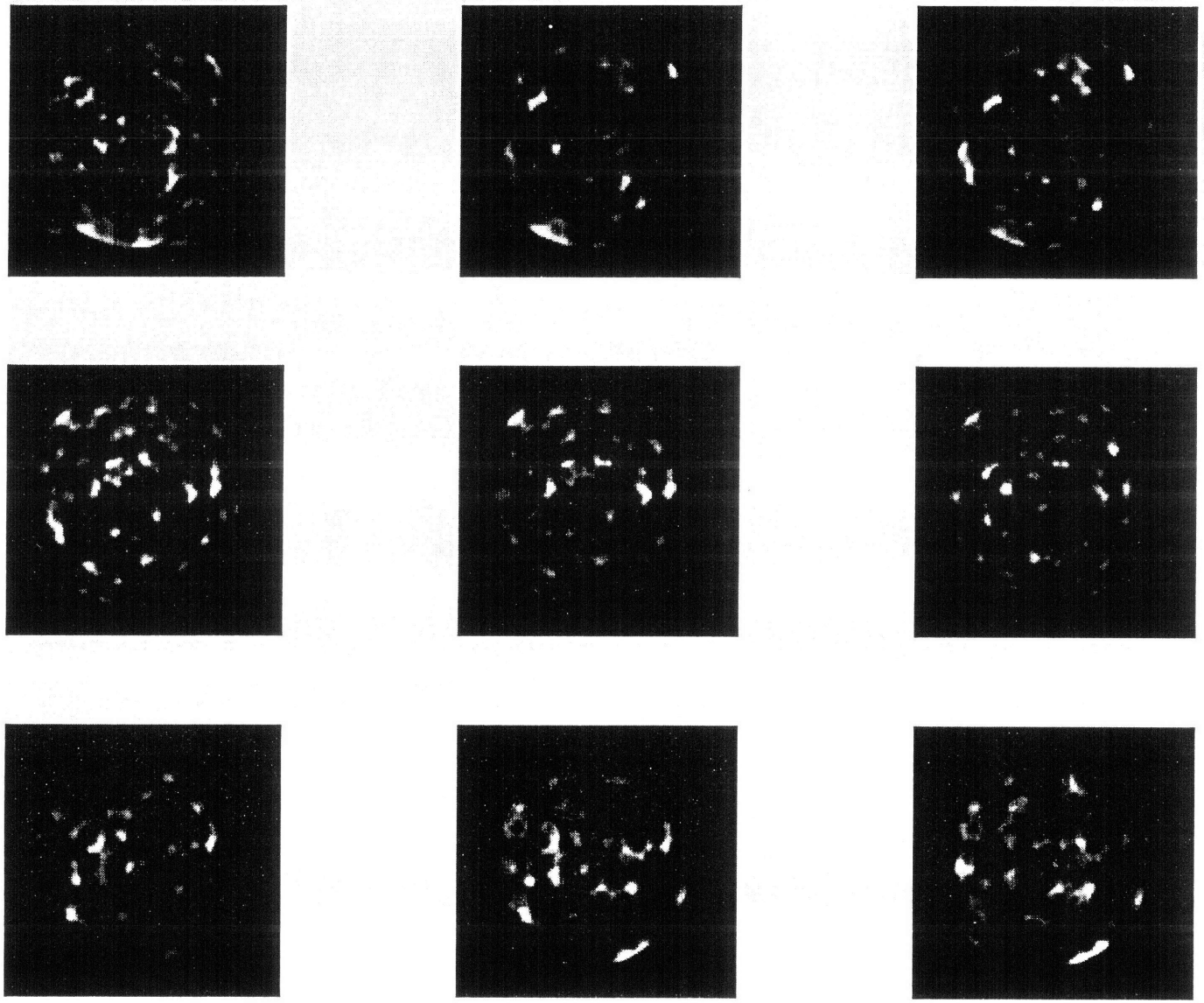

Fig. 7.2(a) images taken at 0.05 mm/sec flushing rate

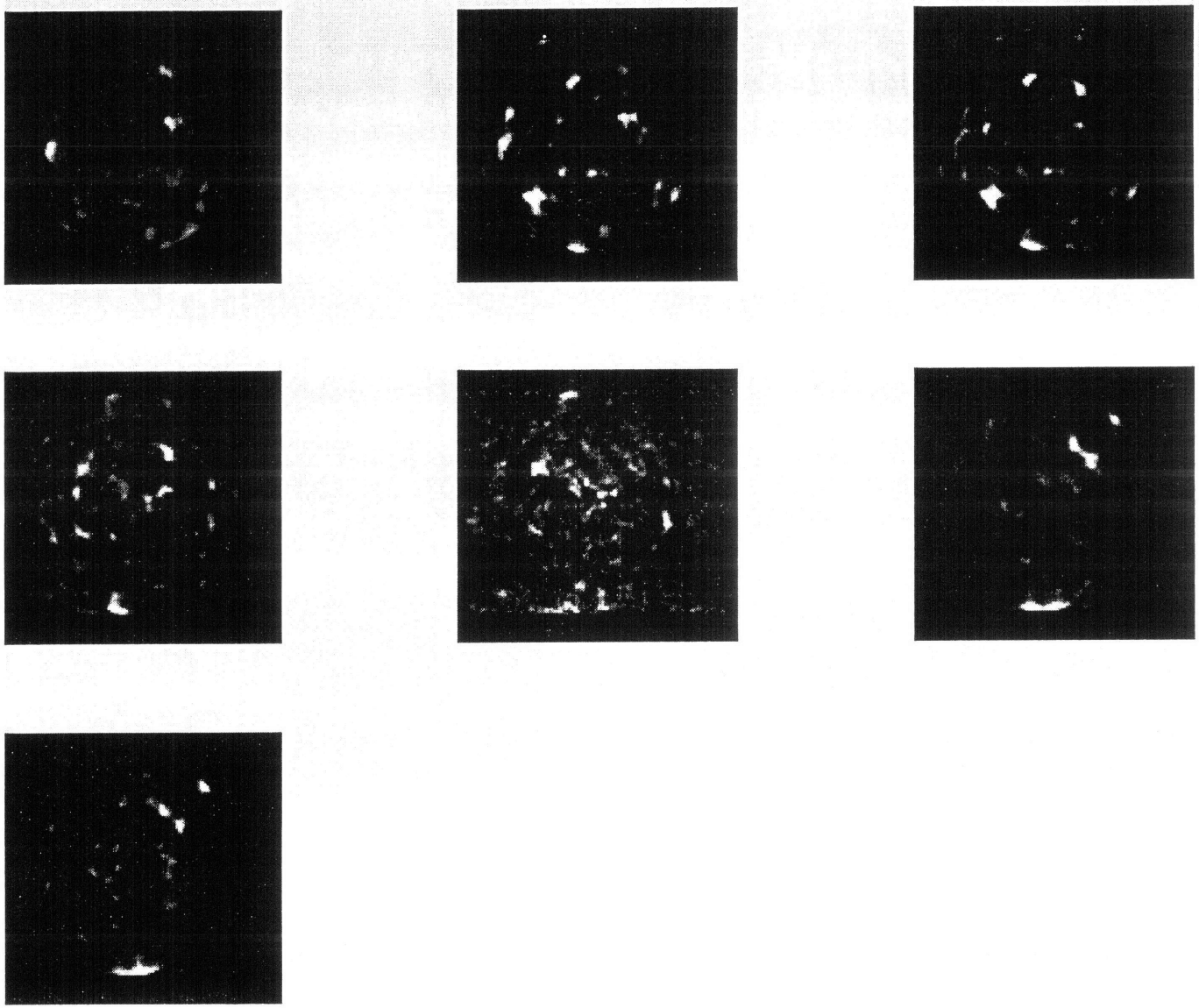

Fig. 7.2(a) images taken at 0.05 mm/sec flushing rate

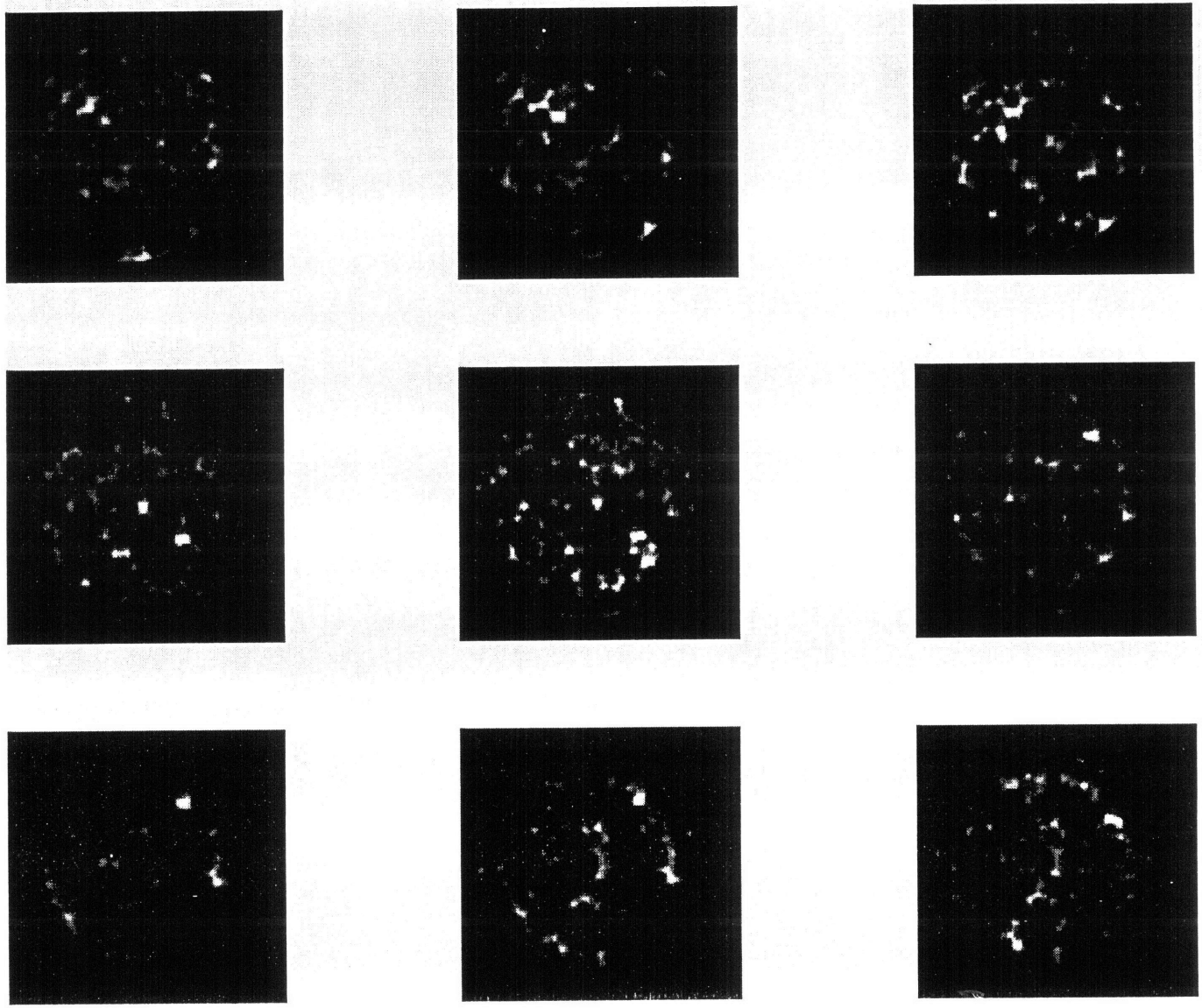

Fig. 7.2(b) images taken at 0.1 mm/sec flushing rate

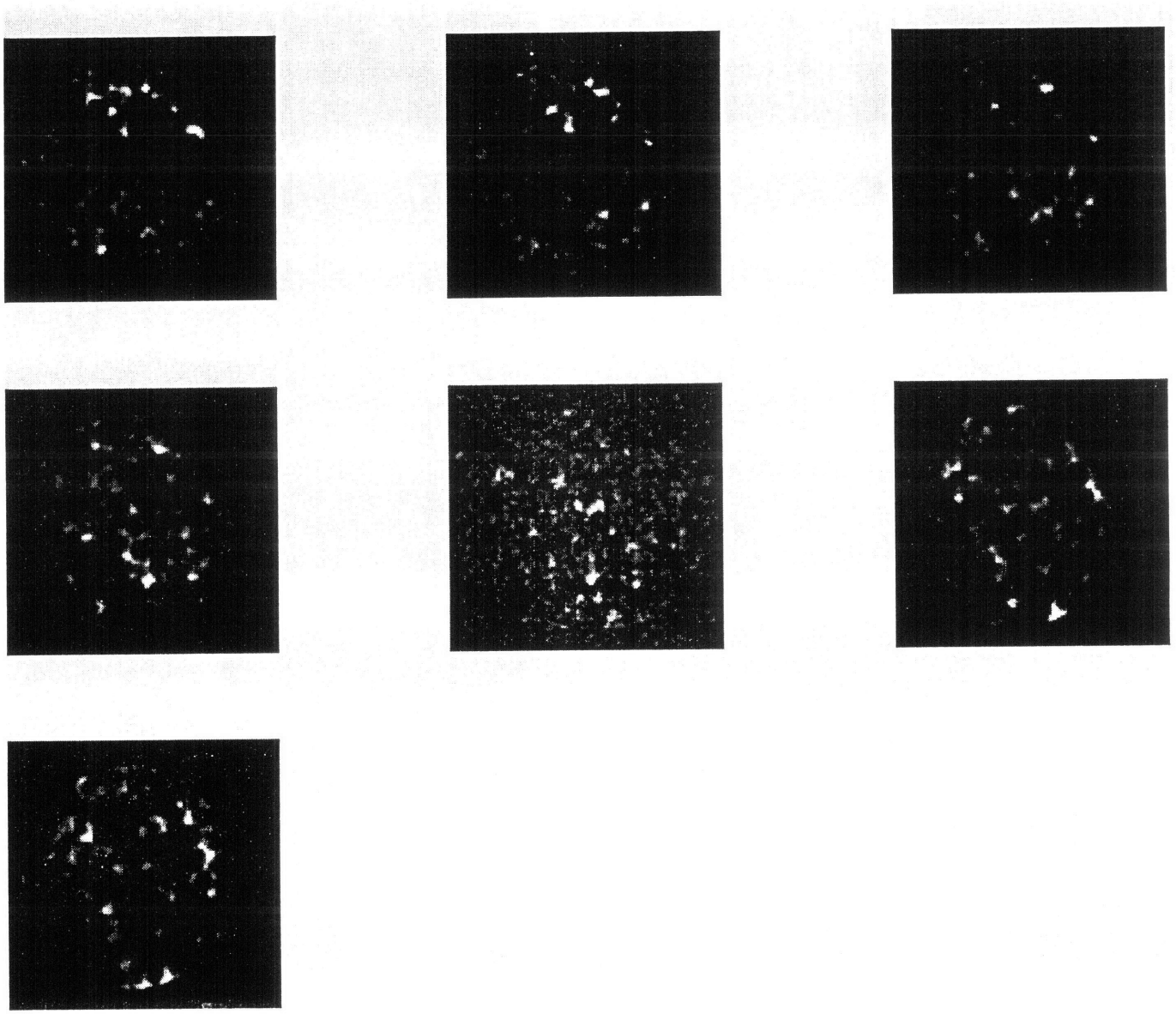

Fig. 7.2(b) images taken at 0.1 mm/sec flushing rate

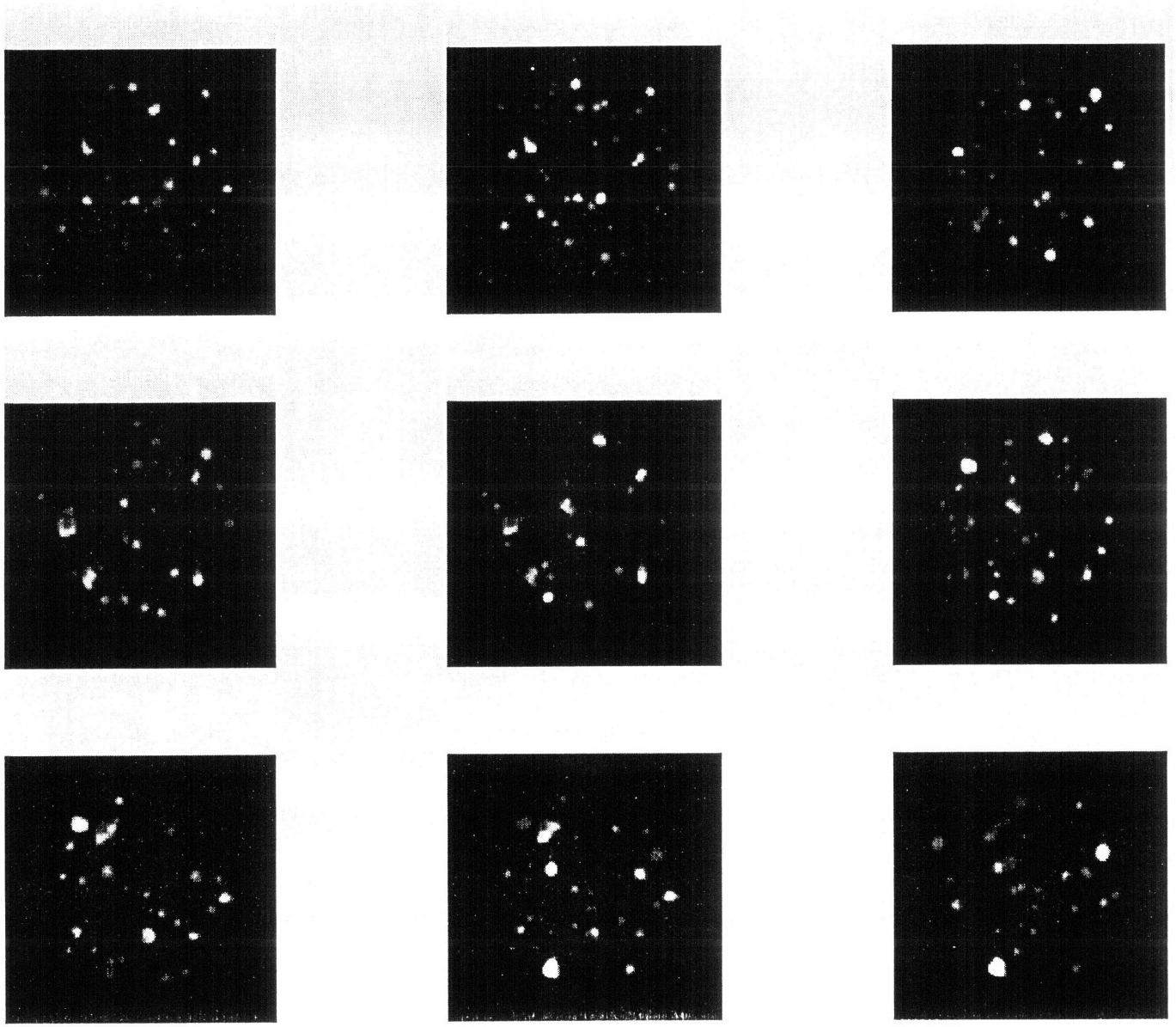

Fig. 7.2(c) images taken at 0.5 mm/sec flushing rate

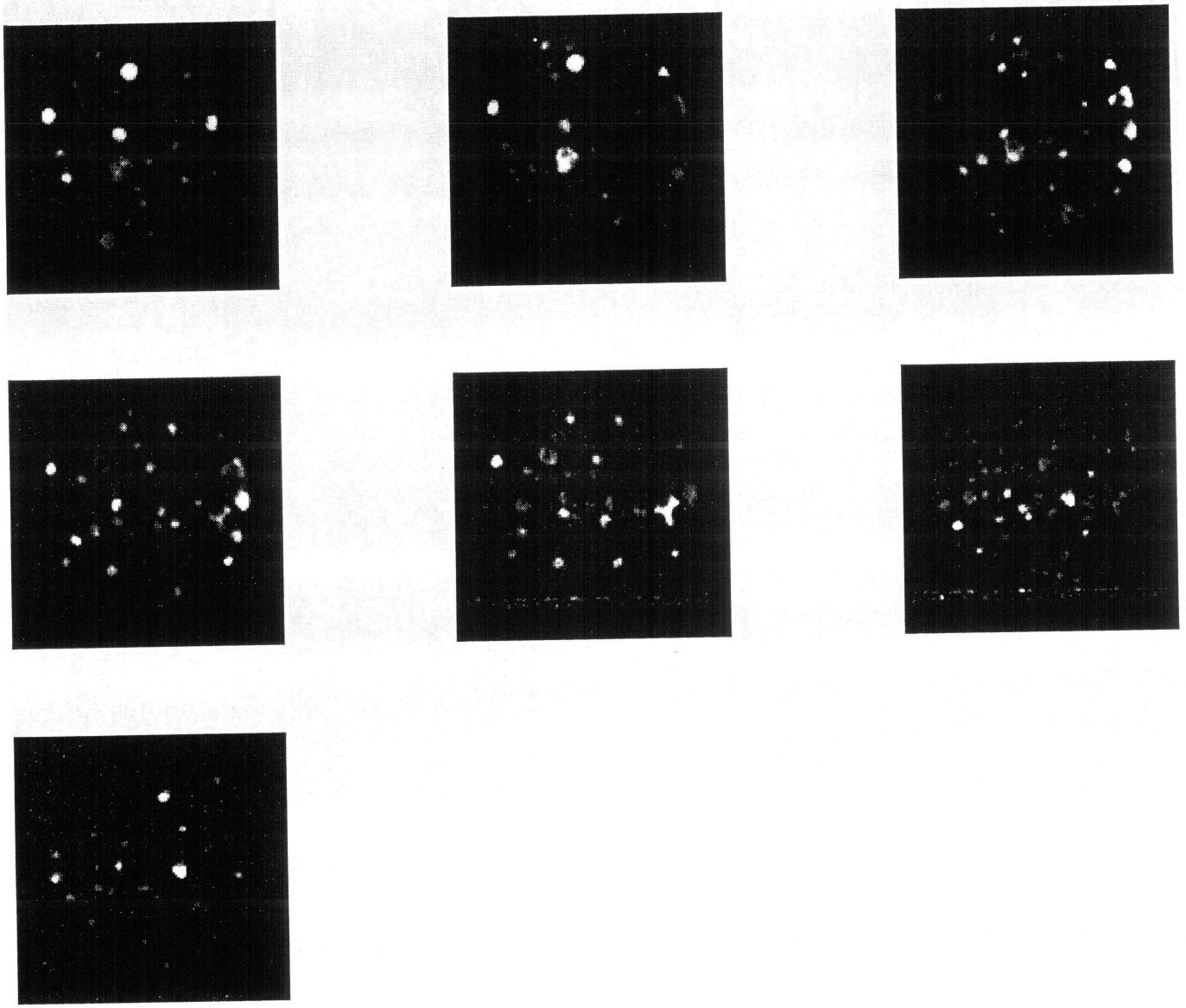

Fig. 7.2(c) images taken at 0.5 mm/sec flushing rate

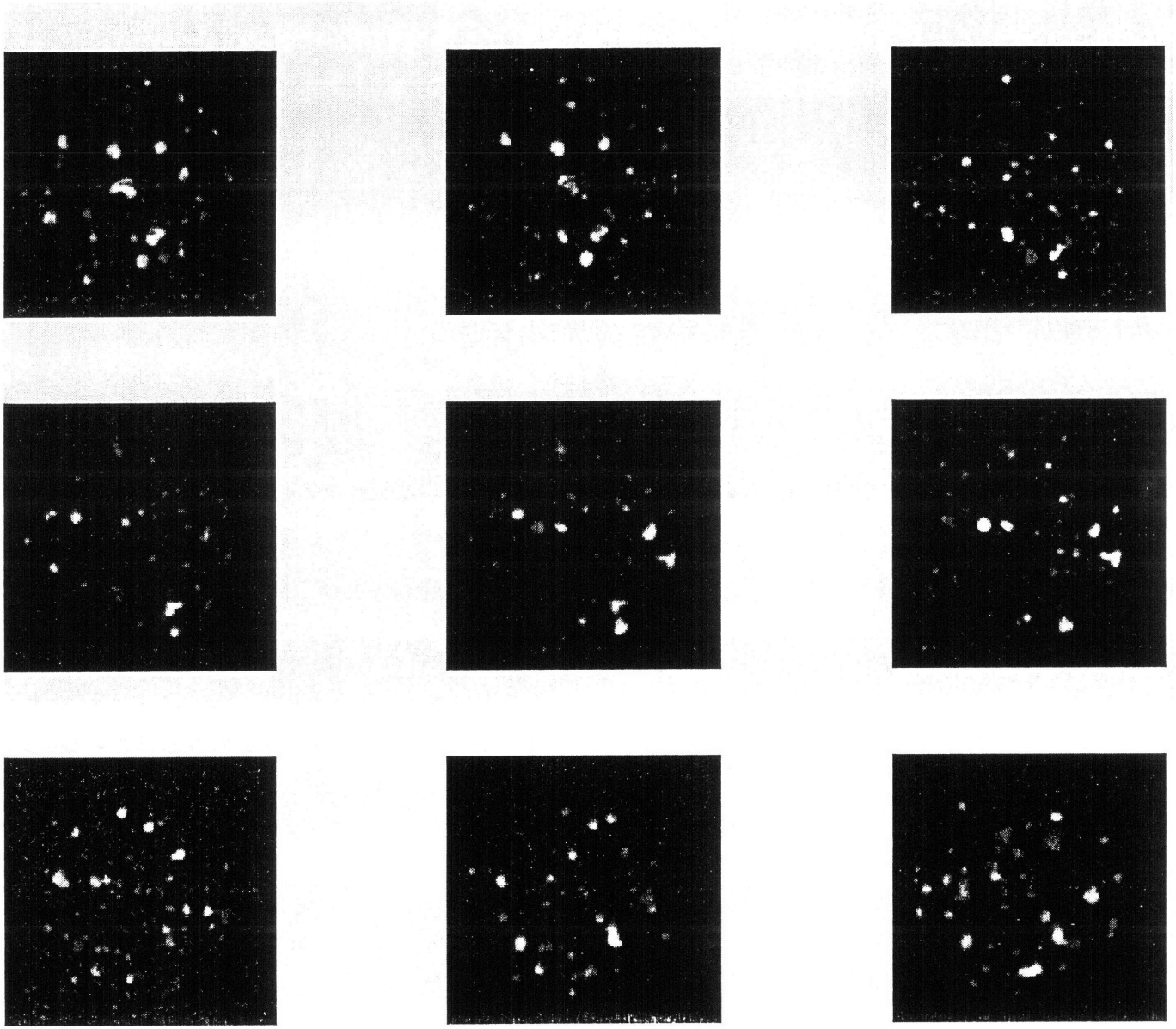

Fig. 7.2(d) images taken at 1 mm/sec flushing rate

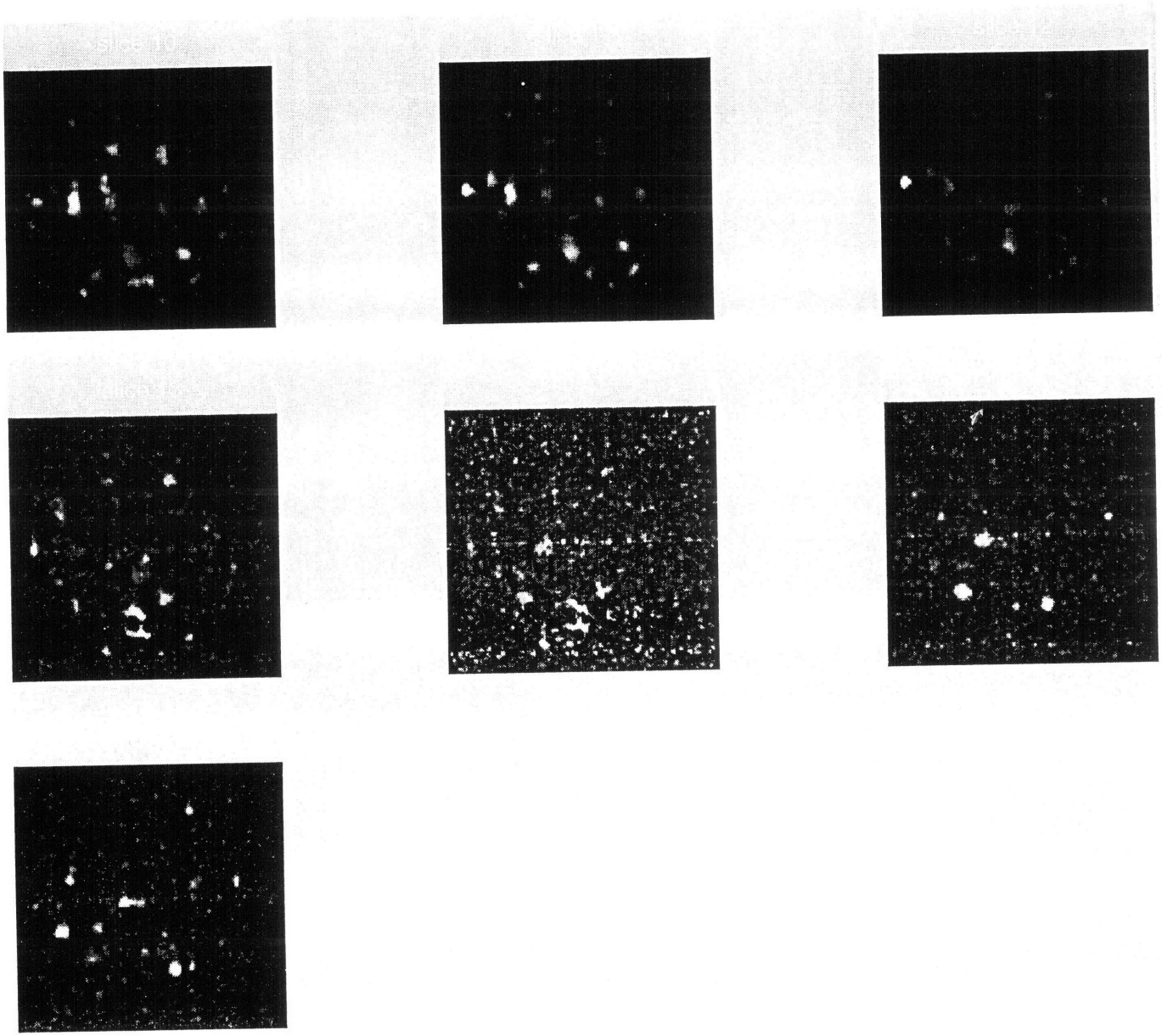

Fig. 7.2(d) images taken at 1 mm/sec flushing rate

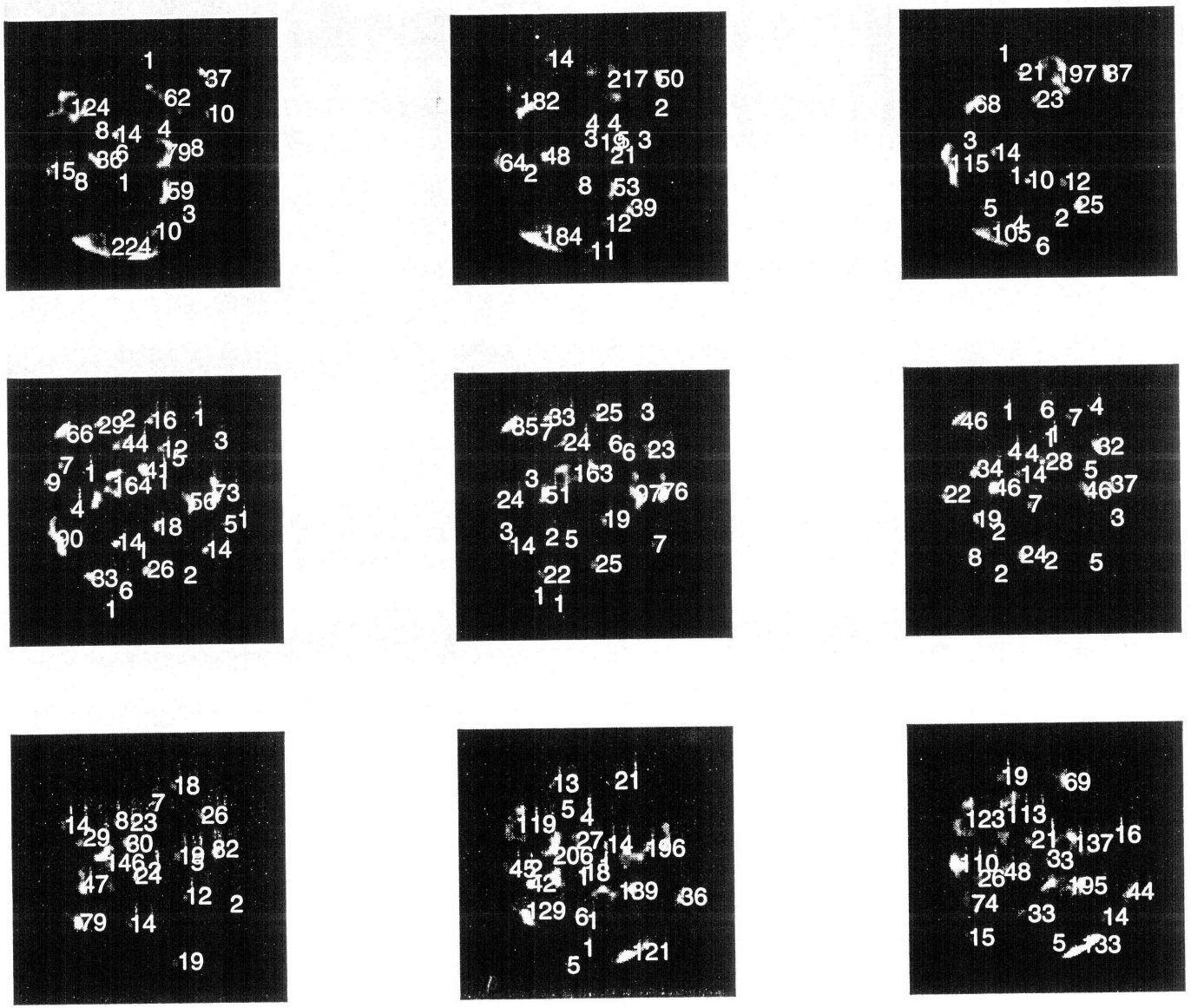

Fig. 7.3(a) digitized images at 0.05 mm/sec flushing rate
(numbers give number of voxels, 1 voxel = 0.00676 mm^3)

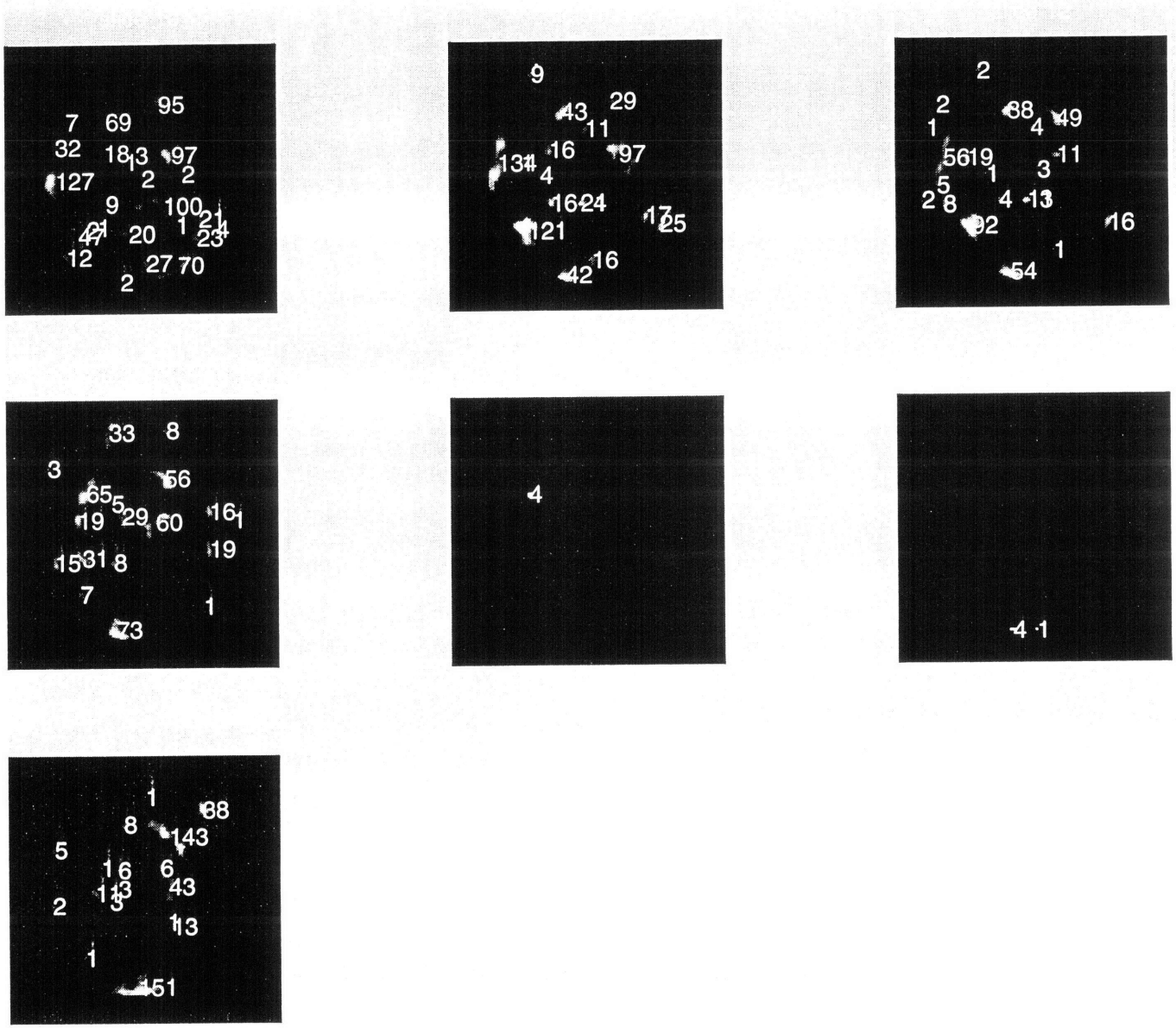

Fig. 7.3(a) digitized images at 0.05 mm/sec flushing rate
(numbers give number of voxels, 1 voxel = 0.00676 mm^3)

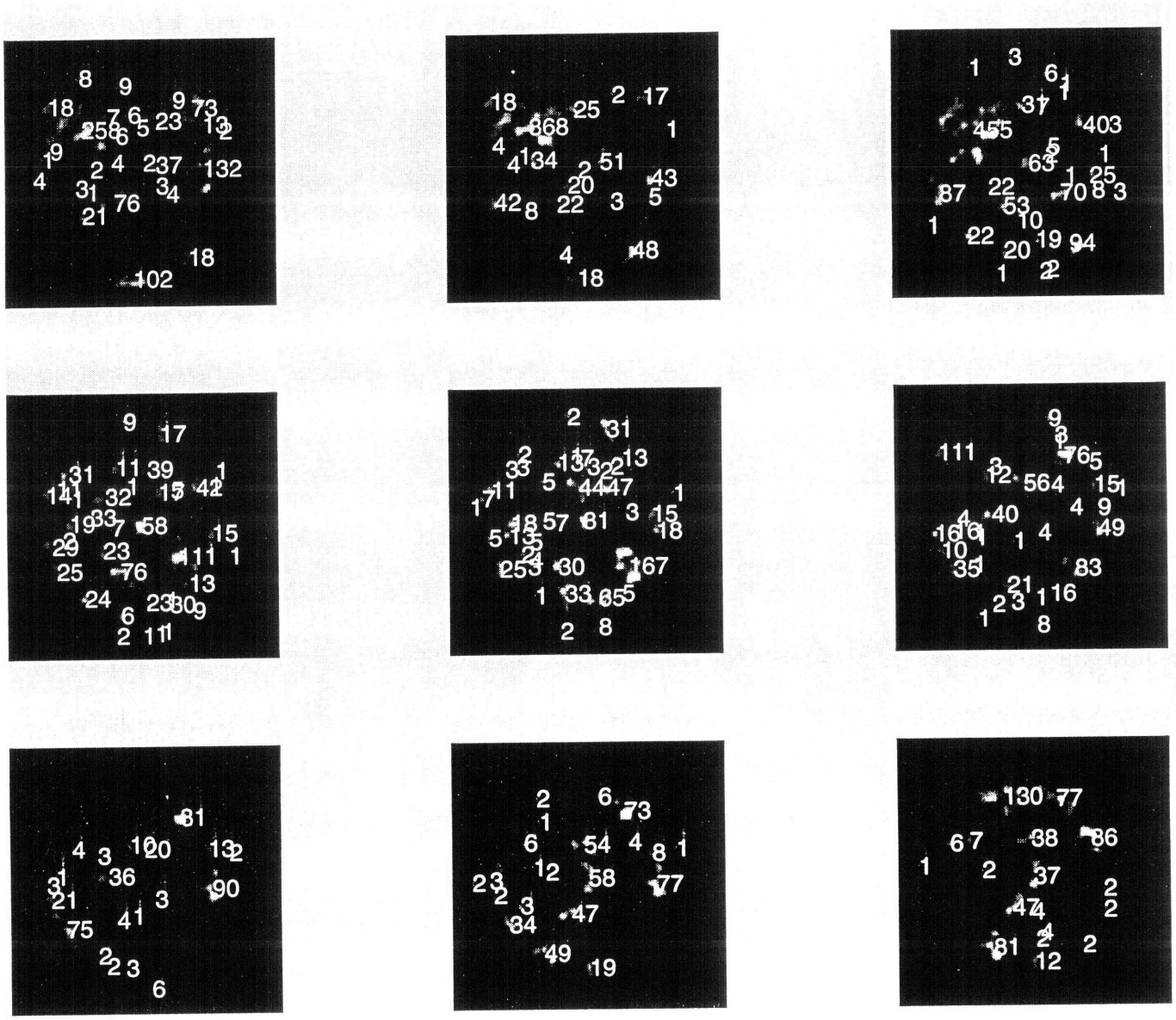

Fig. 7.3(b) digitized images at 0.1 mm/sec flushing rate
(numbers give number of voxels, 1 voxel = 0.00676 mm^3)

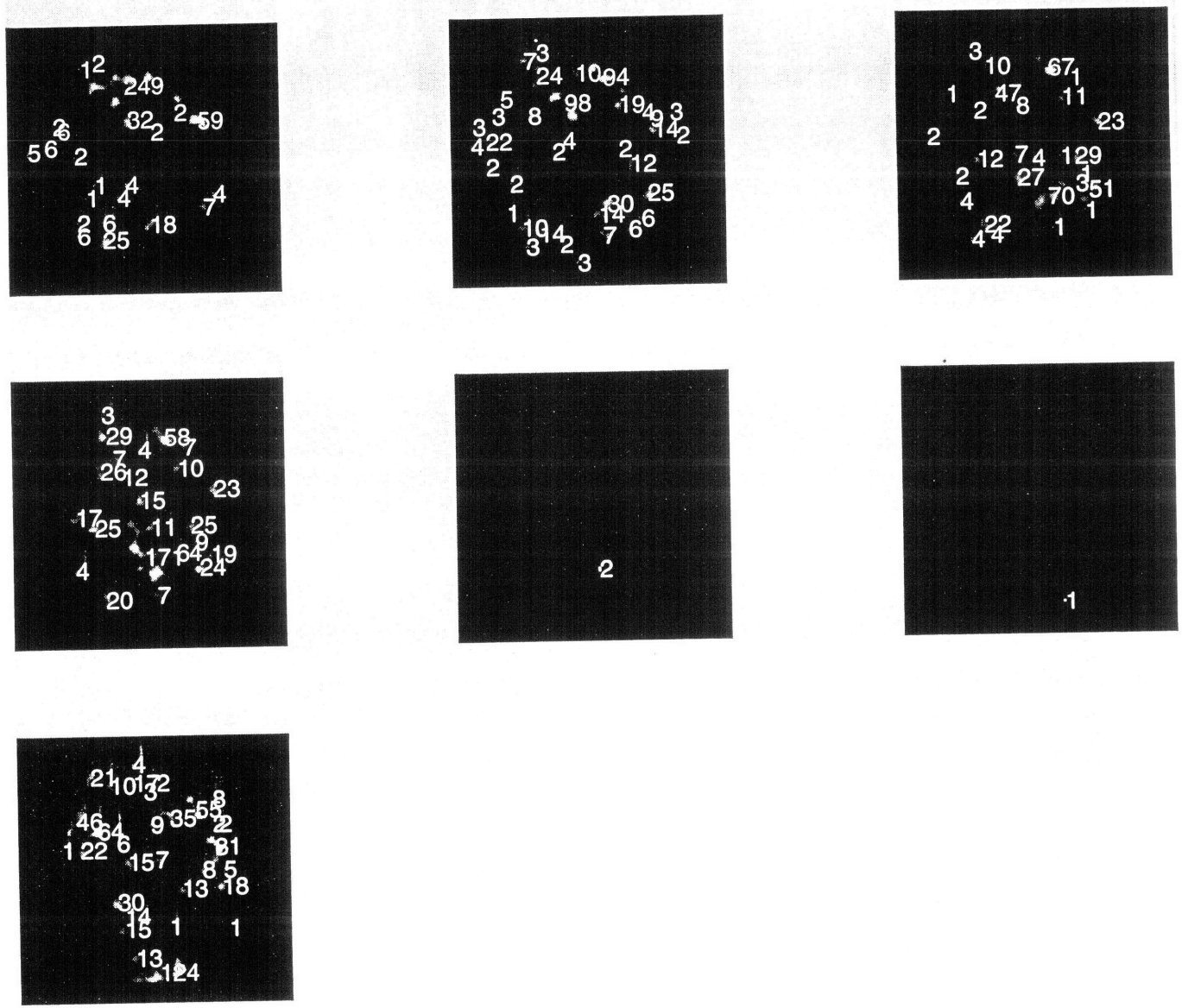

Fig. 7.3(b) digitized images at 0.1 mm/sec flushing rate
(numbers give number of voxels, 1 voxel = 0.00676 mm^3)

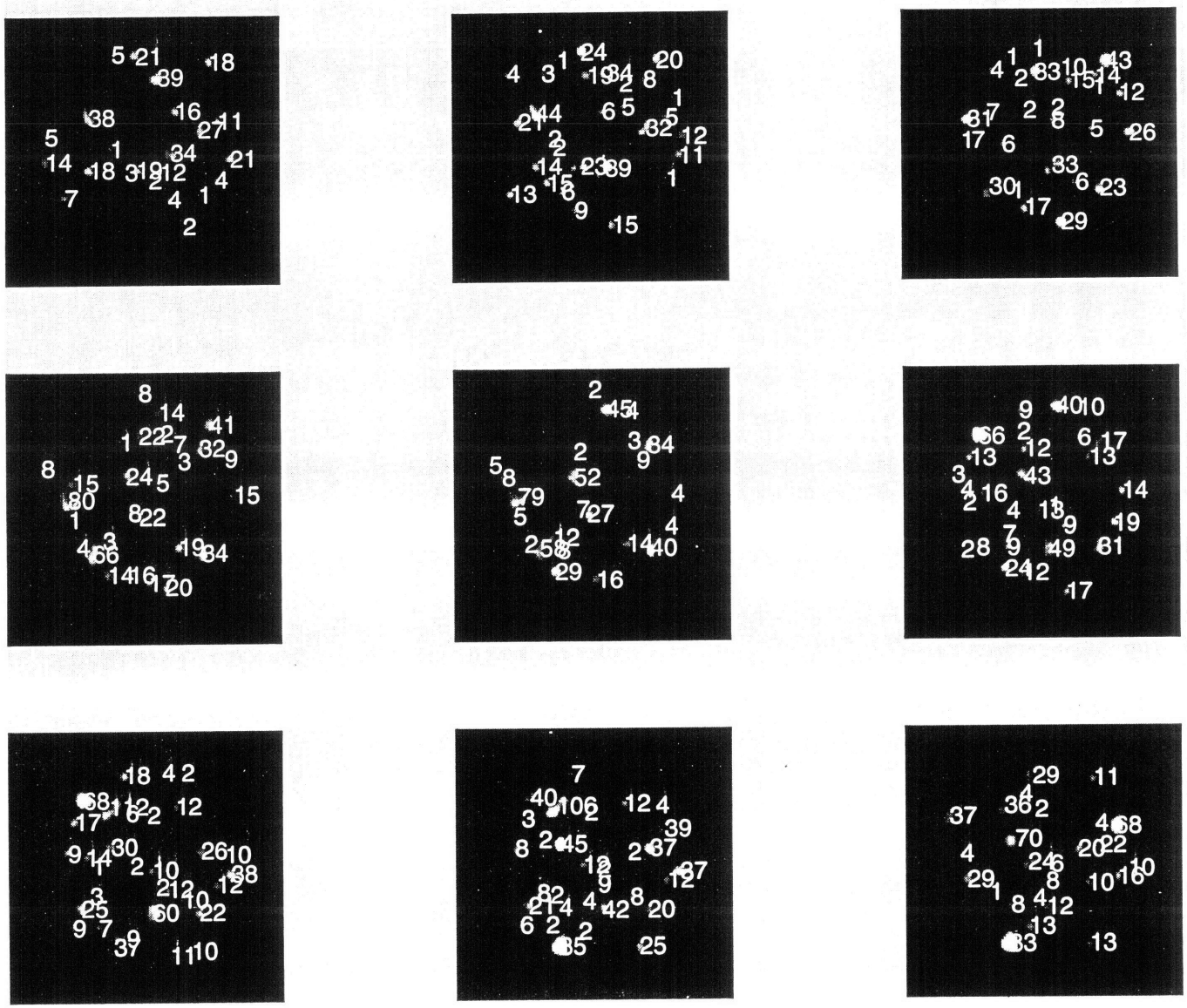

Fig. 7.3(c) digitized images at 0.5 mm/sec flushing rate
(numbers give number of voxels, 1 voxel = 0.00676 mm^3)

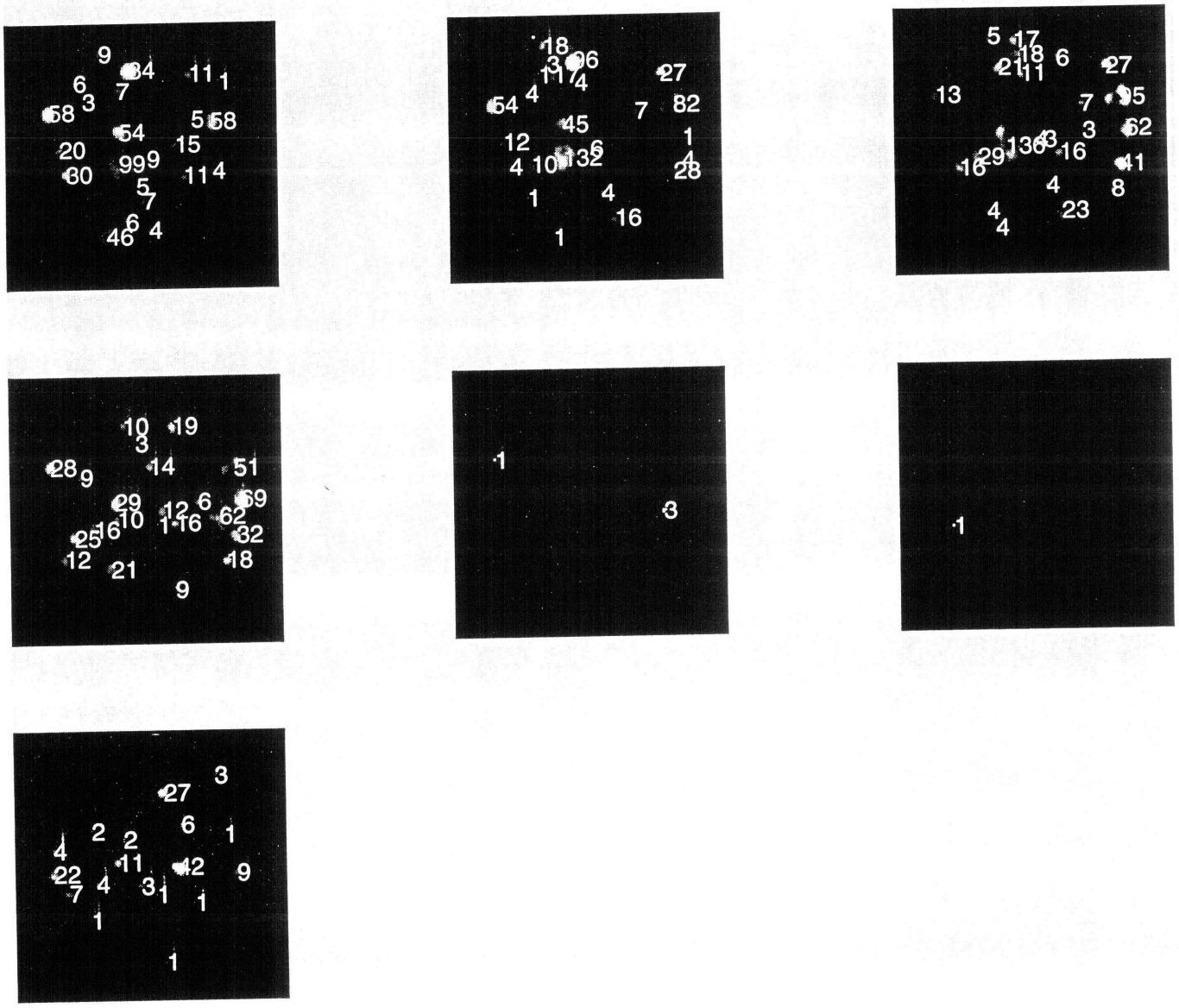

Fig. 7.3(c) digitized images at 0.5 mm/sec flushing rate
(numbers give number of voxels, 1 voxel = 0.00676 mm^3)

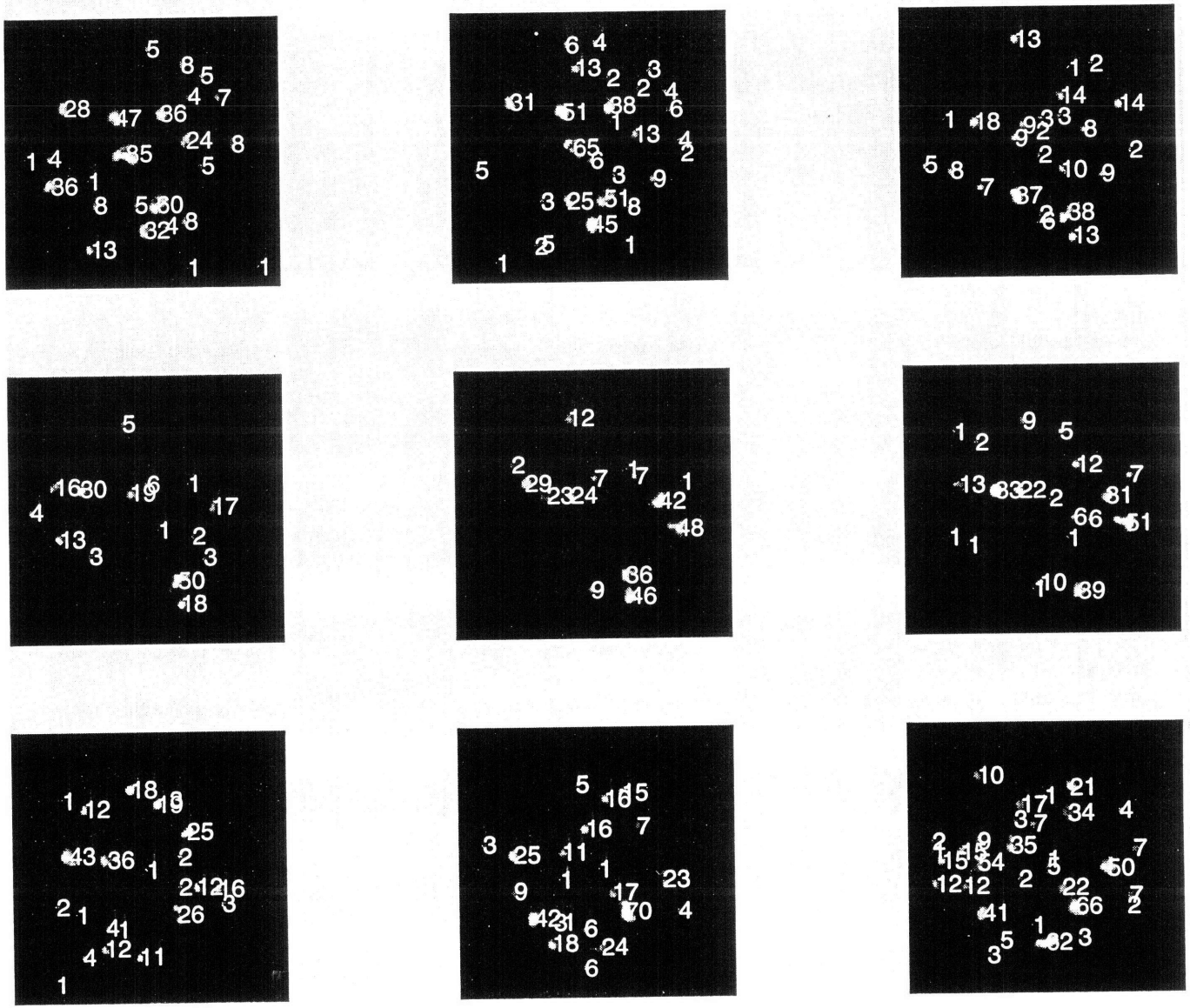

Fig. 7.3(d) digitized images at 1 mm/sec flushing rate
(numbers give number of voxels, 1 voxel = 0.00676 mm^3)

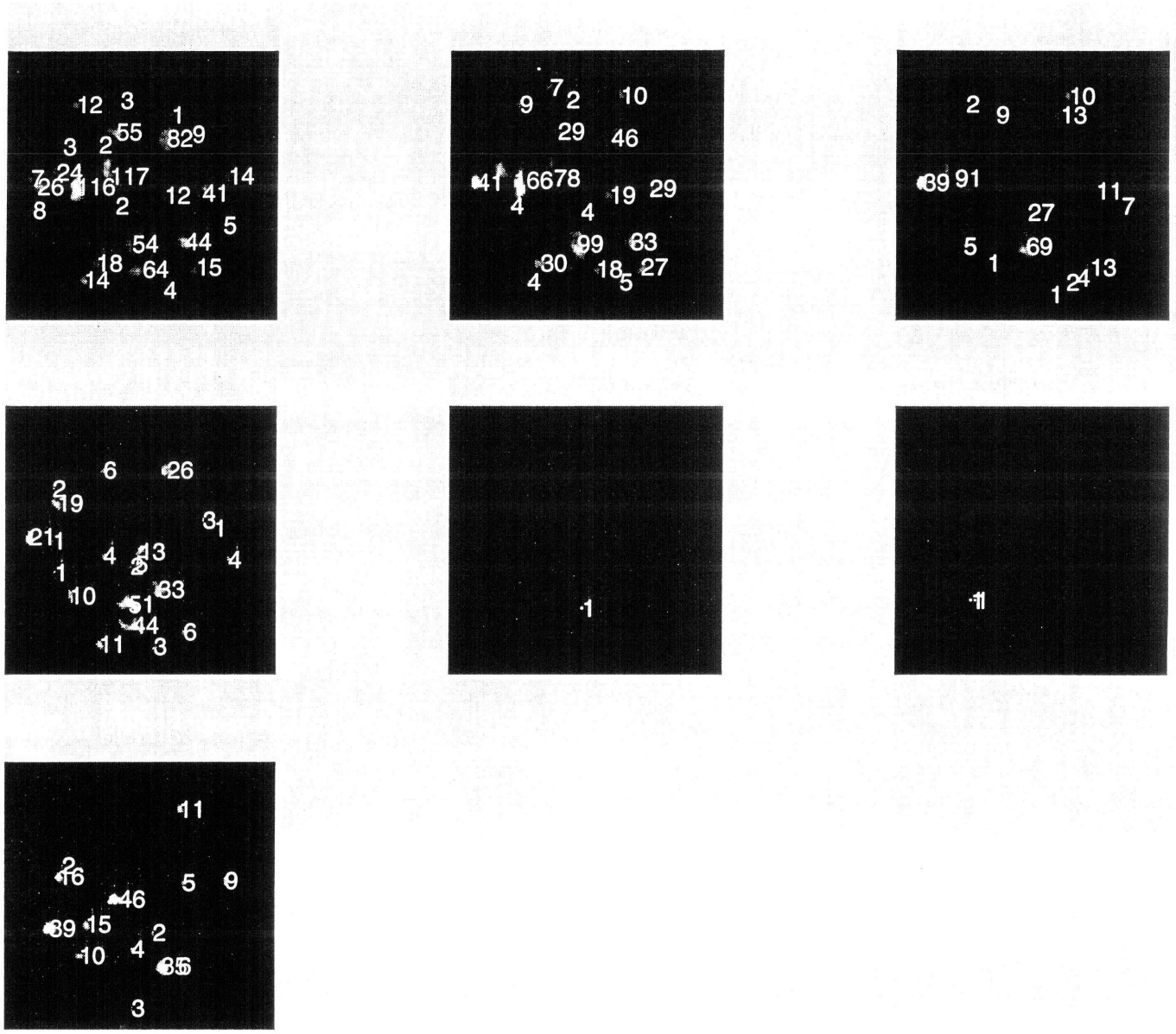

Fig. 7.3(d) digitized images at 1 mm/sec flushing rate
(numbers give number of voxels, 1 voxel = 0.00676 mm^3)

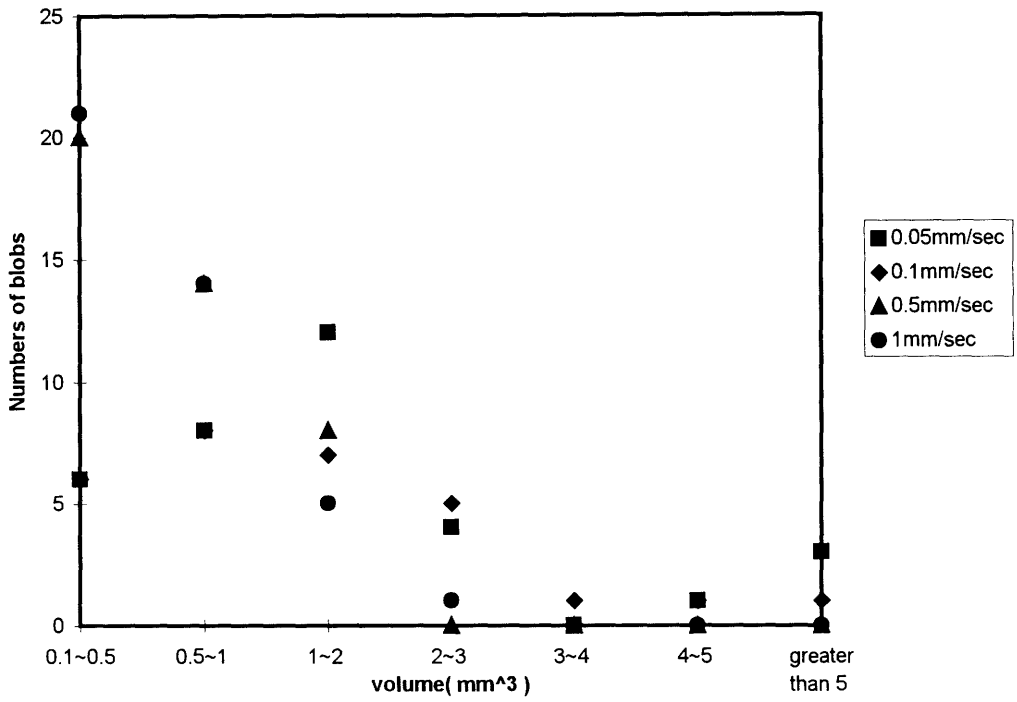

Fig. 7.4 Entrapped oil droplet volume and numbers at different flushing velocities

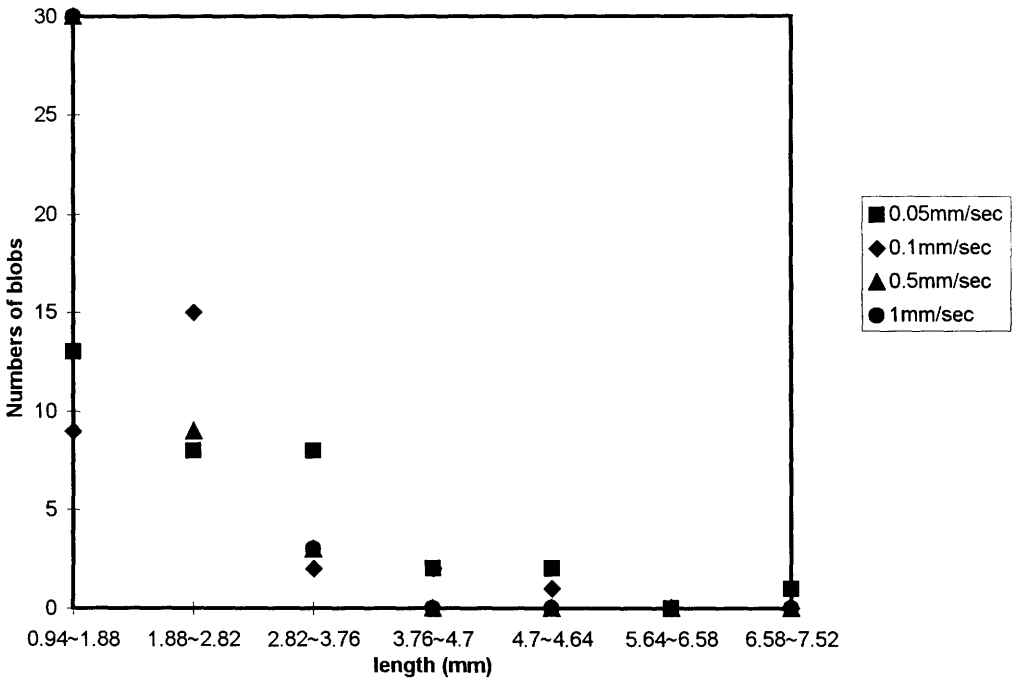

Fig. 7.5 Entrapped oil droplet length and numbers in different velocities

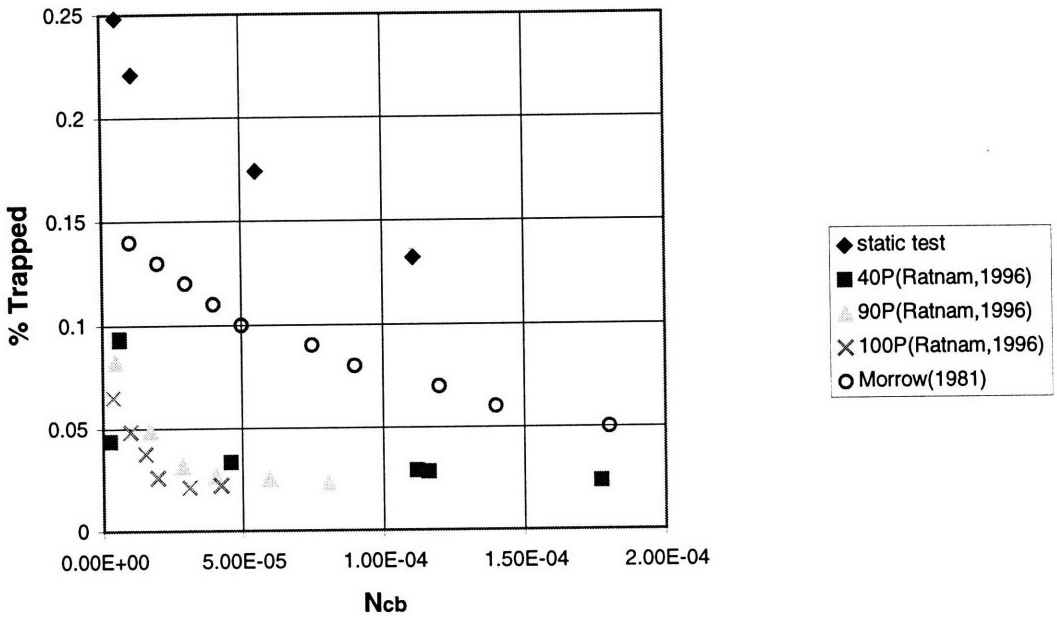

Fig. 7.6 Static tests compared with data from Ratnam (1996b) and Morrow and Sankran(1981)

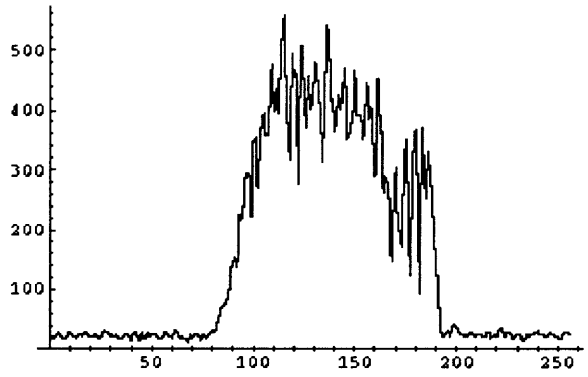

example: 1.vertical axis: intensity of the signal

2. horizontal axis: a.u., which defines the observation window, see Fig. 7.1
3. The D_2O inlet is around 200 a.u., and outlet is around 100 a.u.

Fig. 7.7 The original spectrum due to inhomogenity of coil

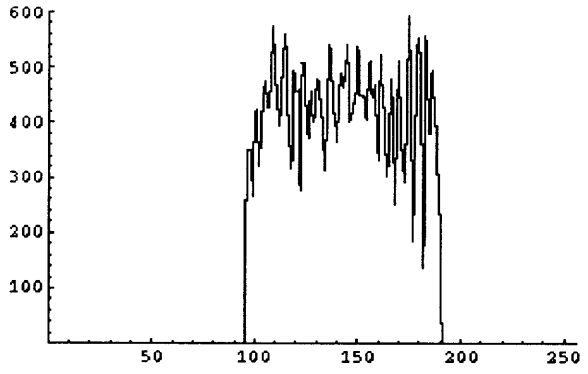

Fig. 7.8 The corrected spectrum

(a)

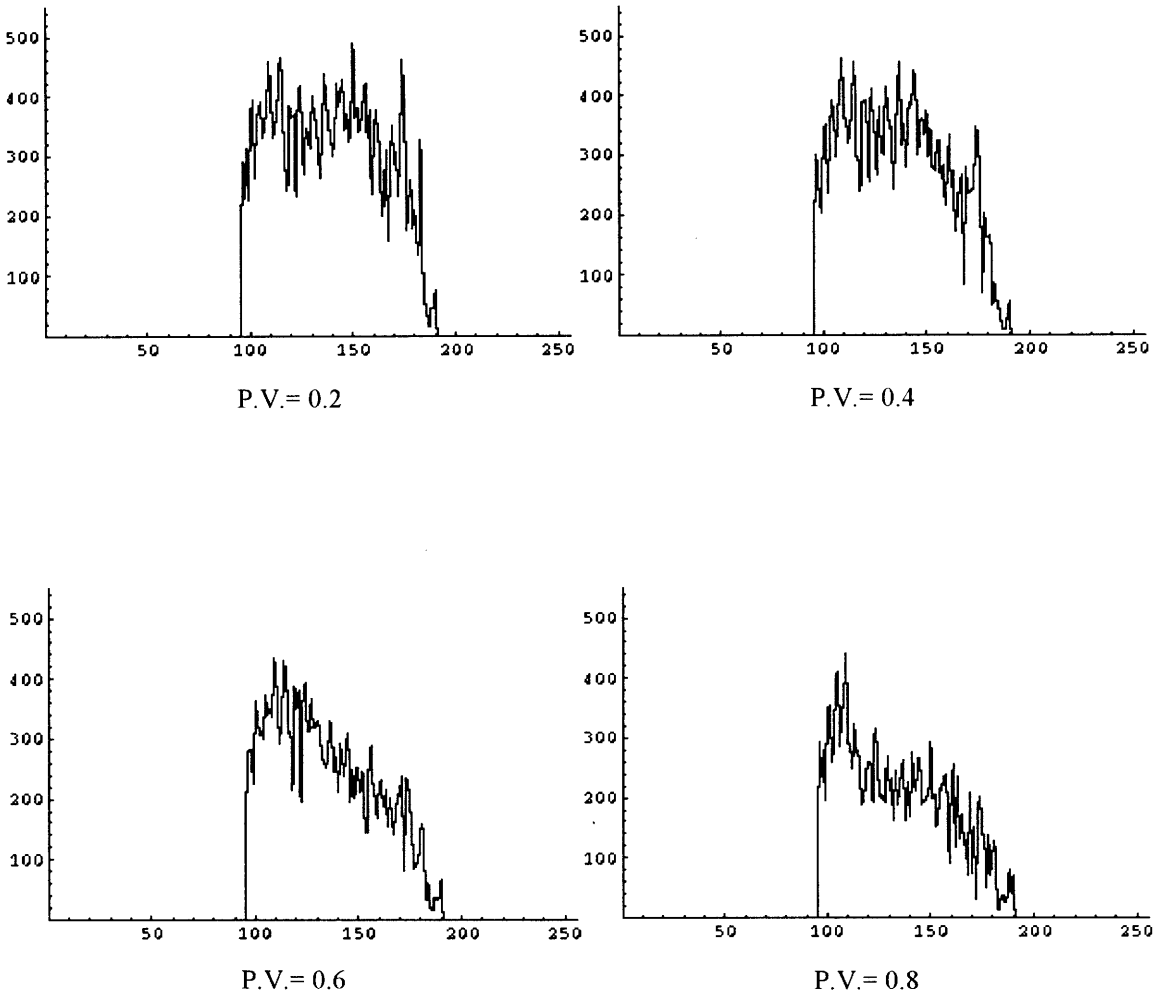

Fig. 7.9 (a) continuous spectrum for V= 0.6 mm/sec (porosity velocity = 1.5 mm/sec)

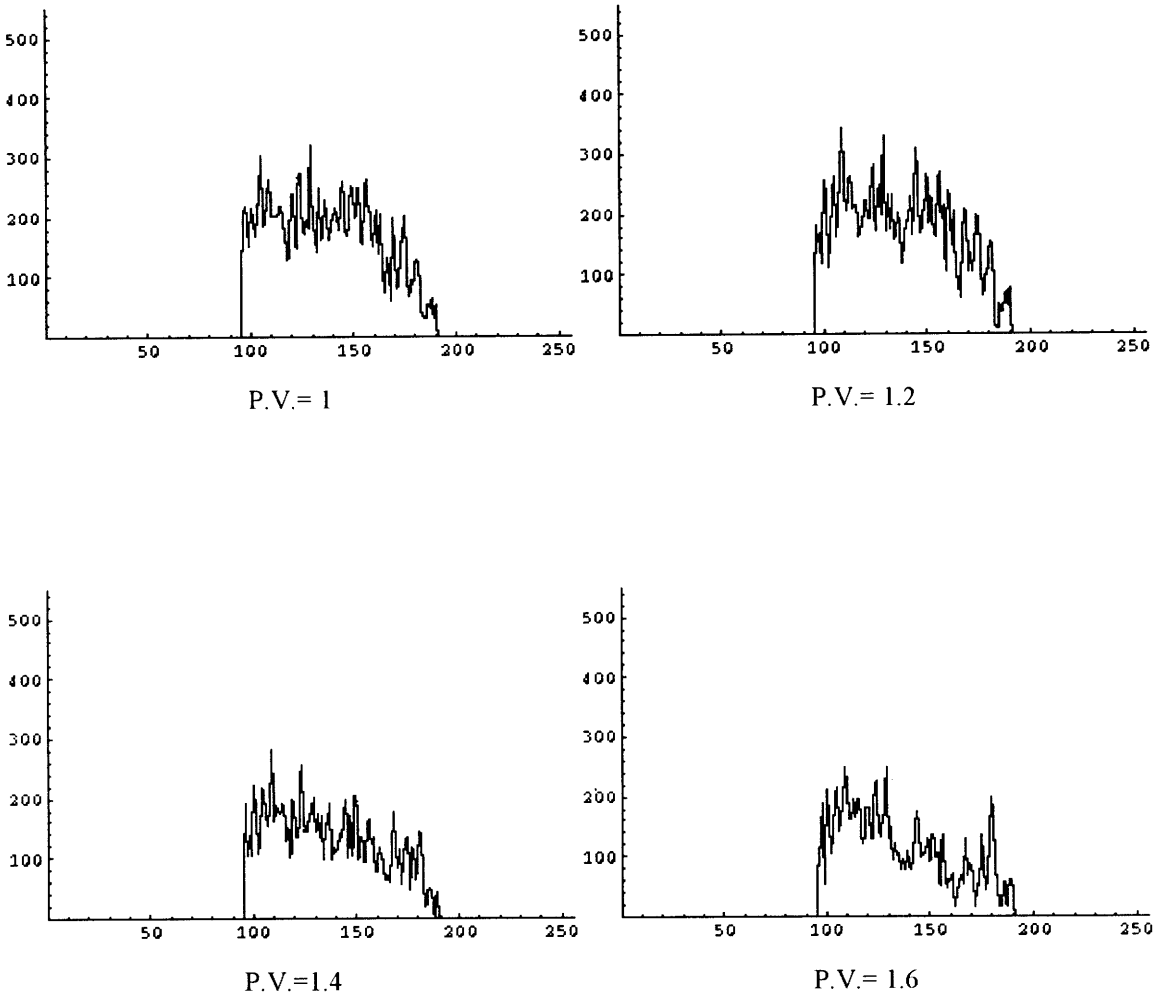

Fig. 7.9 (a) continuous spectrum for V= 0.6 mm/sec (porosity velocity = 1.5 mm/sec)

(b)

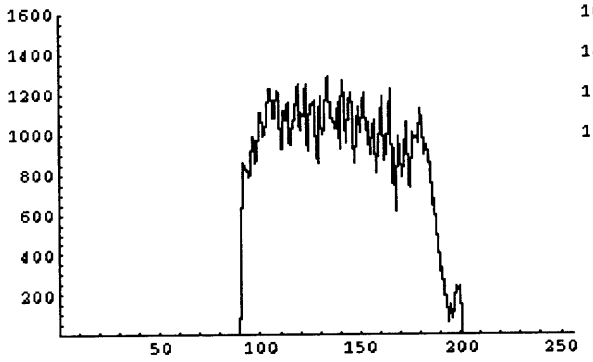

P.V.= 0.2

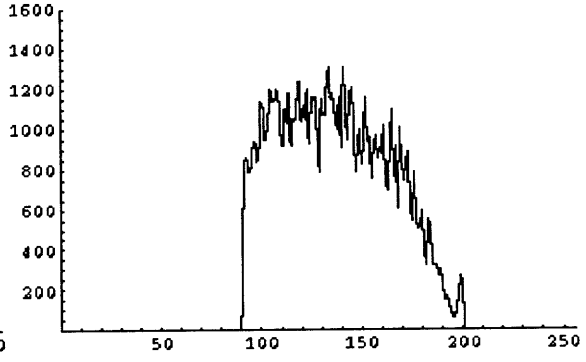

P.V.= 0.4

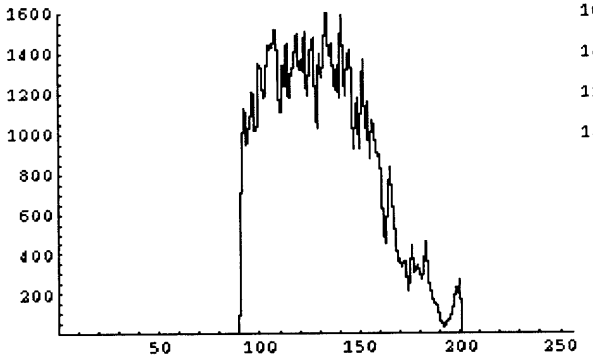

P.V.= 0.6

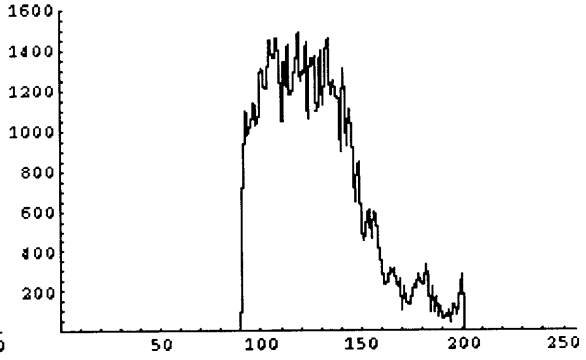

P.V.= 0.8

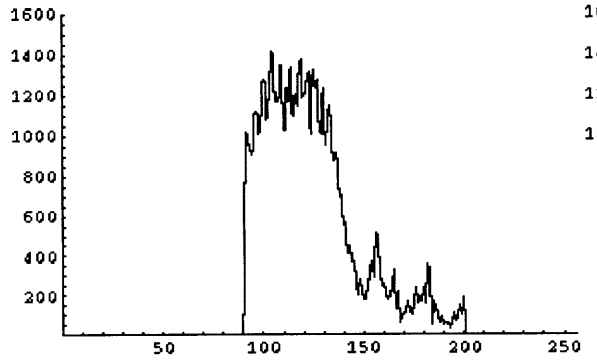

P.V.= 1

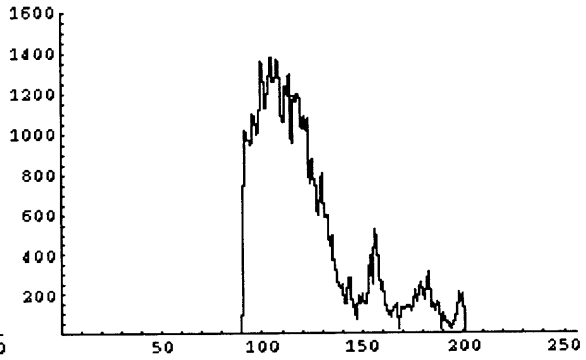

P.V.=1.2

Fig. 7.9 (b) continuous spectrum for V= 3 mm/sec (porosity velocity = 7.5 mm/sec)

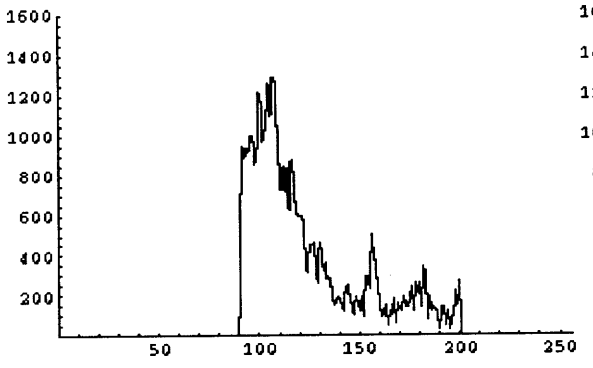

P.V.= 1.4

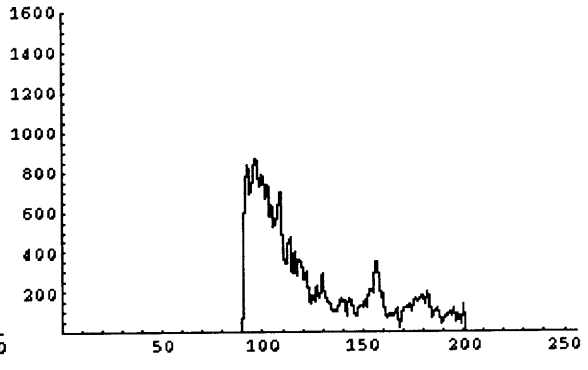

P.V.= 1.6

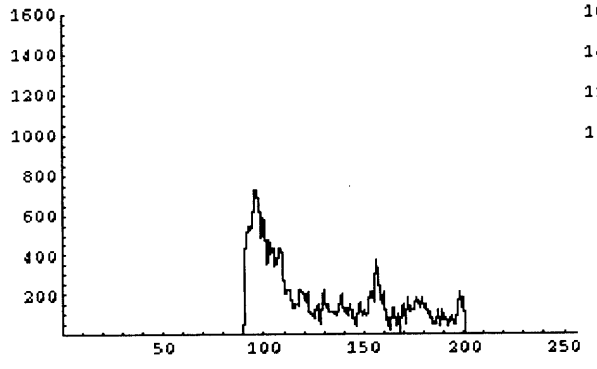

P.V.= 1.8

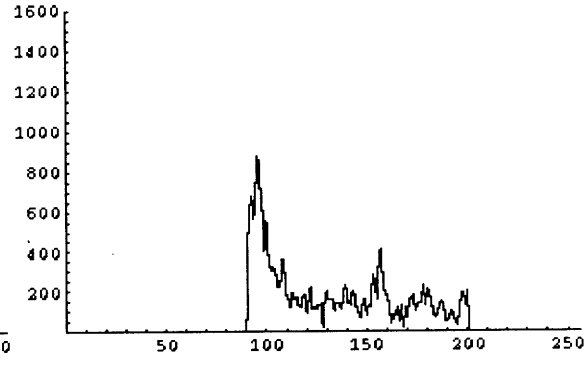

P.V.= 2

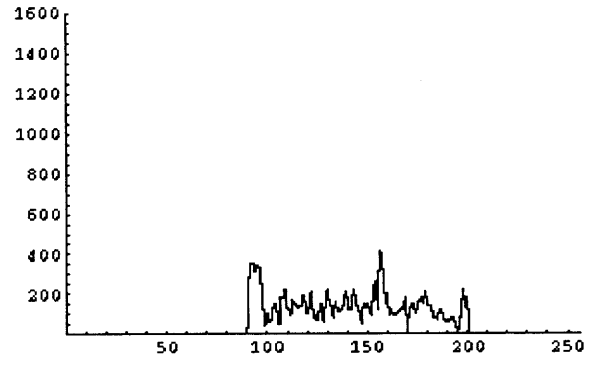

P.V.= 2.2

Fig. 7.9 (b) continuous spectrum for V= 3 mm/sec (porosity velocity = 7.5 mm/sec)

(a)

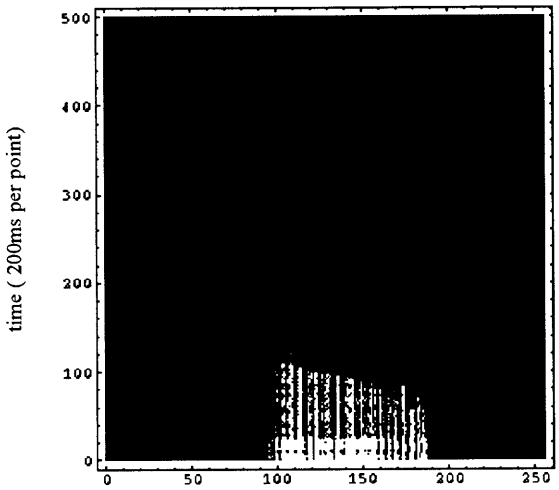

(b)

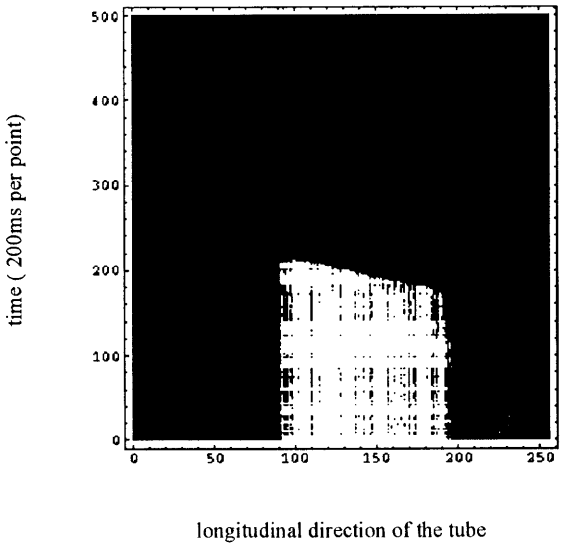

Fig. 7.10 five hundred continuous signals during D_2O flushing (a) flushing velocity: 0.6 mm/sec (b) flushing velocity: 3 mm/sec

(a)

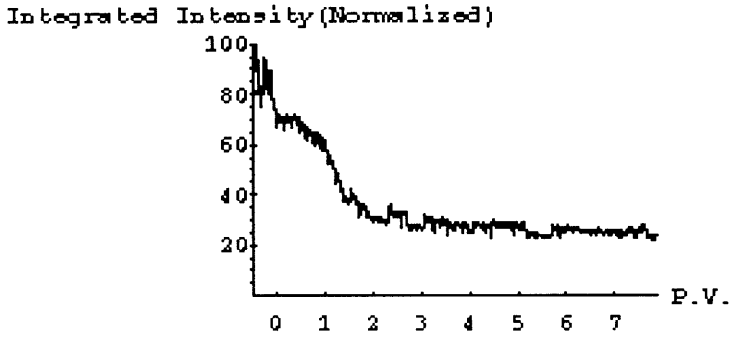

(b)

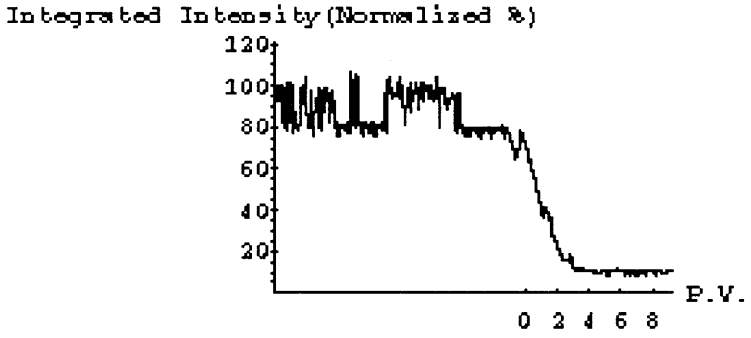

Fig. 7.11 Normalized leftover percentage(a) flushing velocity: 0.6 mm/sec (b)flushing velocity: 3 mm/sec

References

Buckley, J. S. 1991. Multiphase Displacements in Micromodels.. In Interfacial Phenomena in Petroleum Recovery. Marcel Dekker, Inc., New York

Callaghan, P. T. 1995. Principles of Nuclear Magnetic Resonance Microscopy. Oxford science Publication

Chen, J..D., M. M. Dias, S. Patz and L. M. Schwartz, Magnetic resonance imaging of immiscible-fluid diaplacement in porous media, Physical Review Letters, 61(13), 1489-1492, 1988

Crestana, S. and A. N. D. Posadas 1995. 2-D and 3-D Wetting front Instabilities in Layered soils Investigated Through Image Techniques and Invasion Percolation Model. Vadose zone hydrology conference proceedings. University of Calfornia, Davis.

Culligan-Hensley, P. J. 1995. Scaling Immiscible Flow in Porous Media. Personal Communication (not published).

Culligan-Hensley, P. J. Savvidou, C. and Barry, D.A; 1995. Centrifuge Modeling of Transport Processes in Soil- Part 2. Geotechnical News, September.

Culligan-Hensley, P. J. & Savvidou, C. 1995. Environmental geomechanics and transport processes. In Geotechnical Centrifuge Technology. Taylor, R. N. Ed., Blackie.

Culligan-Hensley, P. J. & Savvidou, C. 1994. How can geotechincal engineers contribute to environmental engineering research? Proceeding: The Earth, Engineers, and Education; A Symposium in Honor of Robert V. Whitman. : Dept. of Civil and Environmental Engineering, Massachusetts Institute of Technology. MA

Dereppe, J. M. and C. Moreaux 1991. 2D Spin-Echo and 3D Chemical-Shift-Imaging Techniques for Analysis of Oil-Water Replacement in Limestone. Journal of Magnetic Resonance 91:596-603

Fikushima, E. and B. W. Roeder 1995. Experimental Pulse NMR - A Nuts and Bolts Approach

Foster, W.R. 1973. A Low-Tension Waterflooding Process. Journal of Petroleum Technology: 205-210

Gummerson, R. J. C, Hall, W. D. Hoff, R. Hawkes, G. N. Holland, and W. S. Moore, Unsaturated water flow within porous materials observed by NMR imaging, Nature (London) 281, 56, 1979

Hall, L. D., V. Rajanayagam, and C. Hall 1986. Chemical-shift Imagine of Water and n-Dodecane in Sedimentary Rocks. Journal of Magnetic Resonance 68:183-188

Hall, L. D. and V. Rajanayagam, 1987. Thin-Slice, Chemical-Shift Imaging of Oil and Water in Sandstone Rock at 80 MHz. Journal of Magnetic Resonance 74:139-146

Mace, R. E. and Wilson, J. L. 1991. Clay and Immiscible Organic Liquids: Greater Capillary Trapping of the Organic Liquids: Greater Capillary Trapping of the Organic Phase. Transport and Remediation of Subsurface Contaminants. December

Mandava S. S., A. T. Watson, and C. M. Edwards. 1990. NMR Imaging of Saturation during Immiscible Displacements. AIChE Journal, Vol. 36, No. 11, 1680-1686

Mayer, A.S. and C.T. Miller, 1992. The Influence of Porous Medium Characteristics and Measurement Scale on Pore-Scale Distributions of Residual Nonaqueous Phase Liquids. Journal of Contaminant Hydrology, Vol. 11: 189-213.

Morrow, N.R. 1979. Interplay of Capillary, Viscous and Bouyancy Forces in the Mobilization of Residual Oil. The Journal of Canadian Pet. Technology, Vol. 19:35.

Morrow, N.R. 1991. Introduction to Interfacial Phenomena in Petroleum Recovery. In Interfacial Phenomena in Petroleum Recovery. Marcel Dekker, Inc., New York.

Morrow N. R. & Songkran, B. 1981. Effect of viscous and buoyancy forces on nonwetting phase trapping in porous media. In D. O. Shan (ed), Surface Phenomena in Enhanced Oil Recovery: 387-411. Plenum Press: N. Y.

Ratnam, S., Geotechnical centrifuge modeling of the behavior of light nonaqueous phase liquids (LNAPLS) in sand samples under hydraulic flushing, M. S. Thesis, Massachusetts Institute of Technology, Cambridge, MA, 1996(a).

Ratnam, S., P. J. Culligan - Hensley and J. T. Germaine 1996. The behavior of light, nonaqueous phase liquids under hydraulic flushing. Second International Conference on Environmental Geotechnics, IS-Osaka '96, November 5-8, 1996(b), Osaka, Japan

Stegemeier, G. L. 1976. Mechanisms of Entrapment and Mobilization of oil in porous media. In Improved Oil Recovery by Surfactant and Polymer Flooding. AICHE Symposium. Academic Press, Inc.

Wardlaw, N. C. and M. McKellar, 1985. Oil blob populations and mobilization of trapped oil in unconsolidated packs. Canadian Journal Chemical Engineering: 63, 525-532.

Williams, J. L., A. G. Maddinelli, and D. G. Taylor 1994. Communications: Selective Magnetic Resonance Imagine of Chemicals in Sandstone Cores during Flow. Journal of Magnetic Resonance 109:124-128